

Millimetre wave propagation and scattering phenomena for automotive radar

Nannan Chen

Delft University of Technology

MILLIMETRE WAVE PROPAGATION AND SCATTERING PHENOMENA FOR AUTOMOTIVE RADAR

by

Nannan Chen

in partial fulfillment of the requirements for the degree of

Master of Science

in Electrical Engineering

at the Delft University of Technology,

to be defended publicly on Thursday November 24, 2016 at 15:00 PM.

Thesis committee: Prof. dr. A. Yarovoy, TU Delft
Dr. O. A. Krasnov, TU Delft
Ir. C. M. H. Unal, TU Delft

The work presented was performed at Microwave Sensing, Signals and Systems Group

An electronic version of this thesis is available at <http://repository.tudelft.nl/>.

ABSTRACT

Modern automotive radar operates at the mm-wave frequency band and has to provide reliable sensing information about surrounding targets in all weather conditions. The aesthetic requirements for the modern car design and needs for mechanical protections result in the installation of radar sensor behind different types of plastic cover like the bumper for the forward-looking radar. The influence of radar signal propagation through such dielectric layer, which is a kind of radar radome, usually is taken into account by radar developers and car manufacturers. But during bad weather conditions like rain, this dielectric radome is becoming wet or even covered with a thin layer of water, ice or dirt and the radar signal propagates through the multilayer structure with transmission and reflection characteristics that can be quite different from the single dry radome case. Thus this project is basically focused on water film effects on the wave propagation on the radome and three models, namely a theoretical model fundamentally based on the plane wave propagation on the stratified media, an experimental model based on real measurements and a numerical model based on CST simulation are derived to investigate these effects. In addition, considering the importance of the antenna beam pattern for proper estimation of object angular position, water film effects on the beam distortions are discussed as well.

The radar observation of road signs and other components of road/highway infrastructure can be quite useful sources of information for cars local real-time navigation on the road. To make such observation reliable, the road signs are required to have reasonably big radar cross section in a wide range of observation angles. As the operational wavelength for automotive radar is quite short (about 4 mm), the backscattered signals from road signs can strongly depend on characteristics of the thin layer of the paint on the surface of the objects. Based on these facts, some radar detectable paint samples with special discrete inclusions inside are experimentally studied and the statistical roughness of the surface for each sample is estimated. Such information can be quite useful for the future road or road infrastructure design, aiming to improve objects' detectability with the automotive radar.

ACKNOWLEDGEMENTS

Hereby I would like to express my sincere gratitude to the people helping me and supporting me to finish this project.

Firstly, I would like to thank Dr.Oleg Krasnov who introduced this interesting and challenging thesis topic and supervised me daily in the whole project, giving valuable guidance, suggestions and criticism. Then I would like to thank Prof. dr. Alexander Yarovoy, who provided important recommendations on some parts of the thesis and helped to improve the project work.

Secondly, I would like to deeply thank the PhD student Rossiza Gourova, who always patiently discussed the confusing problems with me and provided meaningful guidance to solve them. Then I would like to thank Dr. Jan Puskely and Ir. Dinh Tran for their contributions to the CST simulations. Besides, I am really appreciated of the experimental supports from Ir. Pascal Aubry and Ing. Fred van der Zwan. I do learn a lot and feel honoured to work with so many talented colleagues in Microwave Sensing, Signals and Systems Group.

Finally, I would like to thank all my family and friends, supporting me and encouraging me during some difficult time.

CONTENTS

List of Figures	ix
List of Tables	xi
1 Introduction	1
1.1 Motivation	1
1.2 Literature review	2
1.3 Contributions, novelties and approaches	3
1.4 Outline of the thesis.	3
2 Wave propagation in stratified media	5
2.1 Wave propagation in stratified lossy media	5
2.2 Dielectric properties of the pure water	8
2.3 Reflectance and transmittance of the single pure water film	11
2.4 Conclusions.	12
3 Theoretical and experimental models for wave propagation on wet radomes	13
3.1 Derivation of the theoretical model for wave propagation on the wet radome	13
3.2 Derivation of the experimental model for wave propagation on the wet radome	16
3.2.1 Experimental settings for measurements of wave propagation on the wet radome	16
3.2.2 Experimental results of reflectance from the backside of the wet radome	18
3.2.3 Experimental results of the transmittance of the wet radome	21
3.3 Comparisons of the experimental and theoretical models	23
3.4 Conclusions.	26
4 Numerical model for wave propagation on wet radomes in CST	27
4.1 Settings for the simulation in CST based on real measurements	27
4.2 Derivation of the numerical model for wave propagation on the wet radome	30
4.2.1 Simulated reflectance from the backside of wet radome in CST	30
4.2.2 Simulated transmittance of the wet radome in CST	33
4.3 Comparisons of the numerical, experimental and theoretical models	34
4.4 Water film effects on the antenna beam pattern (77GHz)	37
4.5 Conclusions.	39
5 Estimation of statistical roughness of the layer surface	41
5.1 Theoretical calculation of the backscatter coefficient for a rough surface	41
5.2 Measurements of the backscattering coefficient of the rough surface	44
5.2.1 Experimental settings	44
5.2.2 Backscattering coefficients of the rough surface based on real measurements	45
5.2.3 Measured backscattering coefficients for three paint samples	46
5.3 Conclusions.	48
6 Conclusions and future work	49
6.1 Conclusions.	49

6.2	Future work	50
A	Determination of the dielectric properties of the radome	51
A.1	Theoretical analysis of the free space technique	51
A.2	Real measurements of the dielectric properties of the radome	52
A.3	Determination of the dielectric constant of the radome	54
B	Numerical model in CST	57
B.1	Modeling of the horn antenna	57
B.2	Modeling of the wet radome	59
C	Script for the theoretical model	61
D	Script for the numerical model	65
	Bibliography	67

LIST OF FIGURES

1.1 Automotive radar applications [1]	1
1.2 Reflectivity from the water film at 76.5GHz at 20°C [2]	2
1.3 Transmissivity through the water film at 76.5GHz at 20°C [2]	2
2.1 Propagation of the plane wave in the lossy stratified media	6
2.2 Dielectric constant of pure water versus frequency estimated from the double-Debye dielectric model (T=20°C)	10
2.3 Dielectric constant of pure water versus temperature estimated from the double-Debye dielectric model ($f=77\text{GHz}$)	10
2.4 Reflectance from the single water film versus thickness (T=20°C, normal incidence)	11
2.5 Transmittance of the single water film versus thickness (T=20°C, normal incidence)	11
3.1 The formed thickness of the water film for a spherical radome with 0.1m/0.3m/0.5m radius versus rain rate	13
3.2 The theoretical model of wave propagation on the wet radome	14
3.3 Theoretical reflectance from the backside of the radome covered with various thicknesses of the water film	15
3.4 Theoretical transmittance of the radome covered with various thicknesses of the water film	15
3.5 Experimental settings for the measurements of wave propagation on the wet radome	17
3.6 Measured mean reflectance from the backside of radome covered with various thicknesses of the water film	18
3.7 Error bar graphs for the reflectance from the backside of the wet radome among 20 measurements	20
3.8 Variations of measured resonant frequencies of the reflectance from the backside of wet radome among 20 measurements	21
3.9 Measured mean transmittance of the radome covered with various thicknesses of the water film	22
3.10 Error bar graphs for the transmittance of the wet radome among 20 measurements	23
3.11 Comparisons between theoretical and experimental reflectance/transmittance of the wet radome	24
3.12 Theoretical and experimental reflectance and transmittance of the radome covered with 0.095mm thickness of water film	25
4.1 Settings for the simulation in CST based on real measurements	27
4.2 Simulated horn antenna pattern at 77GHz ($\phi = 0^\circ$)	28
4.3 Simulated horn antenna gain response with frequency ($\phi = 0^\circ, \theta = 0^\circ$)	28
4.4 Simulated dielectric constant of the radome in CST	29
4.5 Simulated dielectric constant of pure water (17.5°C) in CST	29
4.6 Variations of simulated resonant frequencies versus the range between the antenna and radome	31
4.7 Simulated mean reflectance from the backside of radome covered with various thicknesses of the water film	32
4.8 Simulated mean transmittance of the radome covered with various thicknesses of the water film	33
4.9 Comparisons of theoretical, experimental and numerical models for wave propagation on the wet radome	35
4.10 Simulated model of water film effects on the antenna beam pattern in CST	37

4.11	Water film effects on the antenna beam pattern	38
5.1	Geometry of the rough surface of a single layer	42
5.2	Dielectric constant (ϵ) dependency of the backscattering from the rough surface for H,V polarization ($\sigma=0.3\text{mm}$, $\ell=0.5\text{mm}$)	43
5.3	Root-mean-square height (σ) dependency of the backscattering from the rough surface for H,V polarization ($\epsilon=8$, $\ell=0.4\text{mm}$)	43
5.4	Horizontal roughness (ℓ) dependency of the backscattering from the rough surface for H,V polarization ($\epsilon=8$, $\sigma=0.3\text{mm}$)	43
5.5	Three radar detectable paint samples for the measurements	44
5.6	Experimental setting for the measurements of backscattering from rough surfaces	45
5.7	Measured backscattering coefficients versus incident angels for sample 1, 2 and 3	47
A.1	Experimental settings for the measurements of the dielectric properties of the radome	52
A.2	Measured phase angles with/without the radome and the corresponding phase shift	52
A.3	Actual phase shift and the corresponding real part of the dielectric constant of the radome	53
A.4	Measured mean reflectance/transmittance of the single radome and the corresponding mean squared errors	53
A.5	Summations of the squared residuals for the reflectance and transmittance over the whole bandwidth	54
A.6	Comparison between the theoretical and measured reflectance and transmittance of the radome	55
B.1	Modeling of the single horn antenna in CST	58
B.2	Modeling of the radome (2.678-0.027j) in CST	59
B.3	Modeling of the water film in CST	59
B.4	Local mesh properties of the water film in CST	60

LIST OF TABLES

2.1	Values of coefficients in equation (2.20) of D3M	9
3.1	Comparisons of theoretical reflectance from the backside of the radome covered with various thicknesses of water film	15
3.2	Comparisons of calculated transmittance of the radome covered with various thicknesses of water film	16
3.3	Comparisons of measured mean reflectance from the backside of radome covered with various thicknesses of water film	19
3.4	Comparisons of measured mean transmittance of the radome covered with various thicknesses of water film	22
4.1	Comparisons of simulated reflectance from the backside of radome covered with various thicknesses of water film	32
4.2	Comparisons of simulated transmittance of the radome covered with various thicknesses of water film	33
4.3	Comparisons of the resonant frequency of the reflectance from three models	36
5.1	Estimated dielectric constants and the statistical roughness for experimental samples	48

1

INTRODUCTION

This introductory chapter provides the reader with the general overview of the thesis. In the first section, the motivation of this thesis project will be addressed. Then a literature review of the water effects on the automotive radar performance is summarized. Furthermore, the main contributions and novelties as well as the approaches for this project are stated. Finally, the outline of the thesis is given.

1.1. MOTIVATION

Nowadays, autonomous driving becomes more and more popular due to its diverse benefits. Automotive radar is the key component in autonomous driving systems, including a wide range of applications shown in Fig.1.1[1]. For a collision warning system, the 77GHz automotive radar sensors can detect and track objects, then automatically adjust the vehicle's speed and distance of the cars ahead. In addition, they may trigger a driver warning of an imminent collision and pose emergency braking intervention. Most of these safety-oriented applications in Fig.1.1 demand high reliability in environmental recognition sensors at any traffic and weather scenarios. Unfortunately, by now such requirements appear not to be met well during the adverse weather.

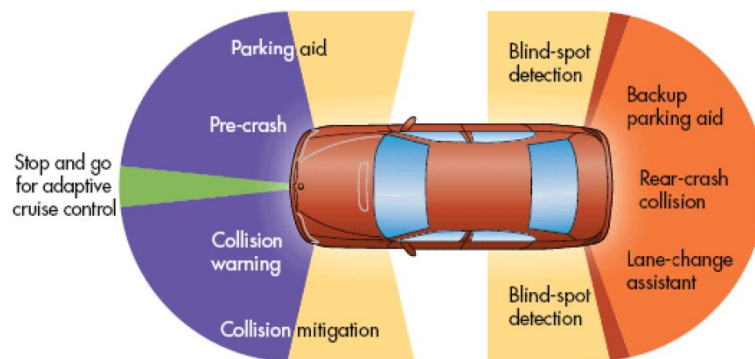


Figure 1.1: Automotive radar applications [1]

The thin water film can be easily formed on the surface of the radome during the adverse weather and causes a considerable loss due to attenuation and reflections. Radar signal propagates through the multi-layer structure with transmission and reflection characteristics that can be quite different from the single dry radome case. As a result, the first part of this project is basically focused on the water film effects on the wave propagation on the radome, including the reflectance from backside of the wet radome which is essential

for the optimal radome design and the transmittance of the wet radome which is associated with the maximum radar detection range. Moreover, considering the importance of the antenna beam pattern for proper estimation of object angular position, the antenna beam distortion due to water film effects is studied as well.

When the radar signal passes the radome/bumper, reaching the road or other components of road/highway infrastructure, the backscattered signals from these objects can be a quite useful source of information for cars local real-time navigation on the road. In order to provide reliable information, the road signs/infrastructures are required to have reasonably big radar cross sections in a wide range of observation angles which is related to the surface roughness of the objects. Thus three radar detectable paint samples are experimentally studied and the statistical surface roughness of each sample is estimated which can be quite useful for the future road or road infrastructure paint design.

With great knowledge of the aforementioned aspects, the future reliability requirements of the automotive radar can be significantly achieved.

1.2. LITERATURE REVIEW

Despite considerable work having been done in the past on analysis and measurements of the effects of water film on micro-wave propagation, the research on the propagation of radar signals specifically operating on 76-81GHz through the dielectric radome covered by water is still rare. By now, the most significant work on the examination of water effects on the automotive radar is from Alebel Arage, a PhD student in the Technische Universit at Darmstadt in 2006. In his dissertation [2], the effects of water film at 76.5GHz on the wave propagation on the radome (proper designed) were investigated. Theoretically the reflectance and transmittance of the wet radome versus thickness of water film were calculated from the fundamental plane wave propagation on the stratified media. Then extensive measurements with the network analyser were performed to validate the theoretical expectations. The calculated and experimental results for co-polarized and cross-polarized cases are shown in Fig.1.2 and Fig.1.3.

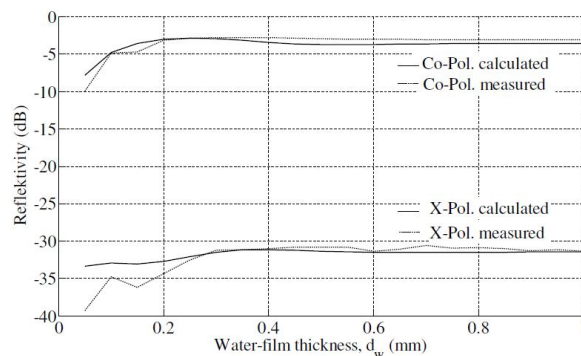


Figure 1.2: Reflectivity from the water film at 76.5GHz at 20°C [2]

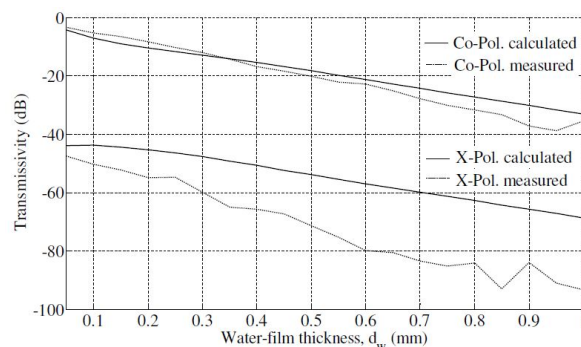


Figure 1.3: Transmissivity through the water film at 76.5GHz at 20°C [2]

As to the water film effects on the antenna pattern around 77GHz, by now, no literature is available. Only the investigation of single bumper effects on the antenna pattern operating at 77GHz is discussed in [3]. In this paper, two parameters for the bumper design have been investigated: 1) the distance between sensor and bumper and 2) the radius of the bumper's curvature. And it is concluded for an optimal performance, the sensor should be mounted as close as possible to the bumper. And the larger the radius of the bumper in front of the sensor, the smaller its influence on the angle estimation.

1.3. CONTRIBUTIONS, NOVELTIES AND APPROACHES

This project investigates the millimetre wave propagation on the radome covered with various thicknesses of water film over the whole automotive frequency band (75GHz~85GHz). To achieve this, three wave propagation models are derived, namely theoretical, experimental and numerical cases. For the theoretical model, it is obtained based on the plane wave propagation on the stratified media. The experimental model is built according to the results from real measurements performed by network analyser. The theoretical model of wave propagation on the wet radome is primarily validated by the experimental model.

Considering the fact that the radome actually is quite close to the automotive sensor (a few centimetres) in the car, and in the real measurements, the distance between the antenna and radome is set to be 3cm only, not fulfilling the far field criterion $R \geq 2D^2/\lambda$. While the theoretical model of wave propagation on the wet radome is derived with the plane wave assumption which deals with the far field. Then the bias between experimental and theoretical model includes the near-field spherical wave effects besides the measurement inaccuracy. Thus a numerical model based on the experimental settings is simulated in CST to further validate the theoretical model. Besides, the water film effects on the antenna beam pattern at 77GHz are studied in CST simulation.

Finally, three radar detectable paint samples with special discrete inclusions inside are experimentally studied and the statistical roughness for the surface of each sample is estimated. Such information can be quite useful for the future road or road infrastructure design, aiming to improve objects' detectability with the automotive radar.

1.4. OUTLINE OF THE THESIS

This master thesis is organized as follows:

- Chapter 2 provides the calculation of wave reflectance and transmittance of the stratified media by applying the propagation matrix approach (PMA). Then, the saline-water double-Debye dielectric model is introduced to obtain the dielectric properties of pure water. Finally, the reflectance and transmittance of a single water film versus the thickness of water film are presented.
- In Chapter 3, primarily the theoretical model of wave propagation on the radome covered with various thicknesses of water film is derived. Then extensive measurements of reflectance and transmittance of the radome covered with various thicknesses of water film are performed and based on the measured results, the experimental model of wave propagation on the wet radome is introduced. Finally, comparisons between these two models are provided.
- Chapter 4 describes the simulated numerical model of wave propagation on the wet radome based on experimental settings. Comparisons among these three models (numerical, experimental and theoretical) are discussed. Moreover, the water film effects on the antenna beam pattern at 77GHz are investigated by the CST simulation.
- In Chapter 5, firstly, the theoretical calculation of backscattering coefficient for the rough surface of a single layer is introduced and discussed. Then the measurements of backscattering from the surfaces of three

radar detectable paint samples at three different frequency bands are performed. Finally, based on the measured results, the statistical roughness of these radar detectable paint samples are estimated.

- Chapter 6 summarizes our findings, conclusions and then some recommendations will be provided for the future work.
- Appendix A describes the measurements of dielectric constant of the radome used for the experiments. Appendix B describes some specific steps for the numerical modeling in CST. Appendix C and D provide MATLAB scripts for theoretical and numerical models.

2

WAVE PROPAGATION IN STRATIFIED MEDIA

Since the thin water film can be easily formed on the surface of the radome by rain drops when the automotive radar is operating in the adverse weather, it is essential to analyse the wave propagation in multiple layers. To achieve this, the propagation matrix approach (PMA) [4] is applied to calculate the wave reflectance and transmittance of the stratified media. Then, the saline-water double-Debye dielectric model is introduced to obtain the dielectric properties of pure water. Finally, substituting the water dielectric into the multilayer wave propagation model, the reflectance and transmittance of a single water film can be estimated before the derivation of theoretical and experimental models of wave propagation on the wet radome discussed in the next chapter.

2.1. WAVE PROPAGATION IN STRATIFIED LOSSY MEDIA

The problem of determining the wave reflected and transmitted at a boundary separating two media can be solved by applying boundary conditions to the solutions of Maxwell's equations. Consider a plane EM wave incident in medium 0 (air) upon a planar boundary between medium 0 and medium 1 shown in Fig.2.1 and the plane of incidence is the plane xOz . Each layer (non-magnetic) is infinite extent and characterized by the constitutive parameters (ϵ_i, μ_0) . Meanings of the notations in Fig.2.1 are described as below:

ϕ_i : Incident angle in medium i ;

d_i : Thickness of medium i [m];

ϵ_i : Relative permittivity of medium i , complex for lossy medium ;

E_i^- : Amplitude of the summation of all the negative-going (reflected) electric field in medium i ;

E_i^+ : Amplitude of the summation of all the positive-going (transmitted) electric field in medium i ;

To examine the wave propagation in the lossy stratified media, the complex propagation constant γ_i in medium i is introduced, where $\gamma_i = j\omega\sqrt{\mu_0\epsilon_0\epsilon_i} = \alpha + j\beta$ [5]. Here α is the medium's attenuation constant and β is the phase constant. When the medium relative permittivity ϵ_i is real, the wave does not suffer any attenuation as it travels (loss-less medium, $\alpha = 0$) and the phase constant β equals to the wave number $k_i = \omega\sqrt{\mu_0\epsilon_0\epsilon_i}$.

For non-normal incidence on an isotropic film, it is necessary to distinguish the wave polarization. The wave of arbitrary polarization can be described as the superposition of two orthogonally polarized waves, one with its electric field parallel to the plane of incidence (parallel polarization) and the other with its electric field perpendicular to the plane of incidence (perpendicular polarization). Here we add the suffix **s** or **p** to denote the perpendicular and parallel polarization respectively. Thus in medium m , the x, y components of the electric and magnetic field can be expressed as :

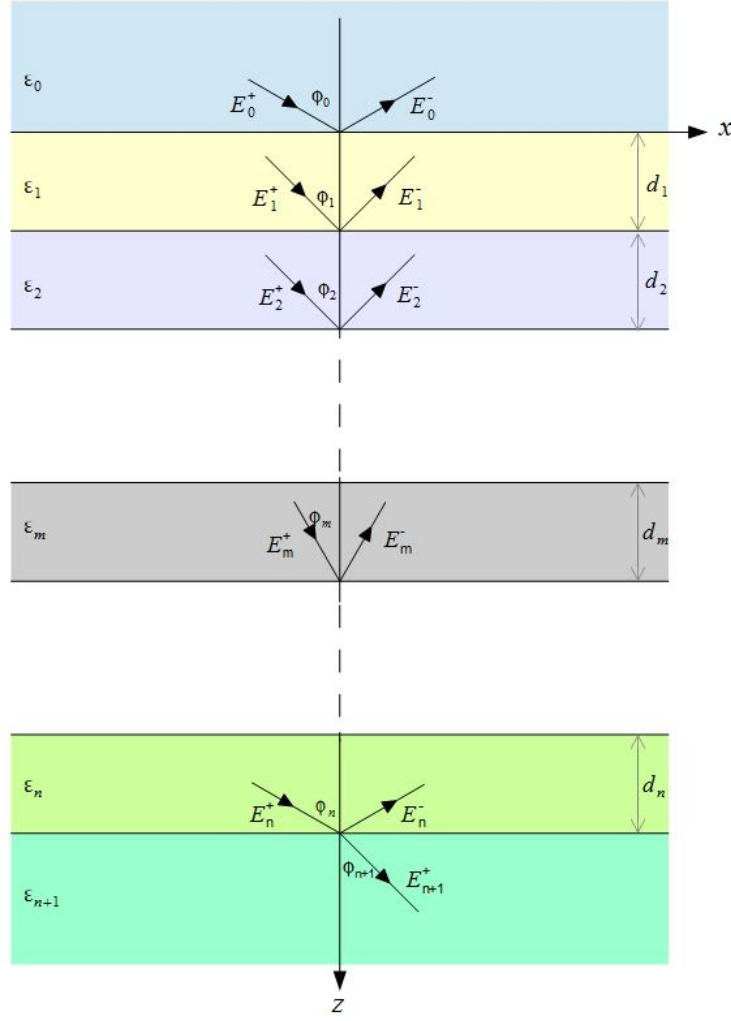


Figure 2.1: Propagation of the plane wave in the lossy stratified media

$$E_{mx} = (E_{mp}^+ e^{-\gamma_m z \cos \phi_m} + E_{mp}^- e^{+\gamma_m z \cos \phi_m}) e^{-\gamma_m x \sin \phi_m} \cos \phi_m \quad (2.1)$$

$$E_{my} = (E_{ms}^+ e^{-\gamma_m z \cos \phi_m} + E_{ms}^- e^{+\gamma_m z \cos \phi_m}) e^{-\gamma_m x \sin \phi_m} \quad (2.2)$$

$$H_{mx} = (-E_{ms}^+ e^{-\gamma_m z \cos \phi_m} + E_{ms}^- e^{+\gamma_m z \cos \phi_m}) e^{-\gamma_m x \sin \phi_m} \sqrt{\epsilon_m} \sqrt{\epsilon_0 / \mu_0} \cos \phi_m \quad (2.3)$$

$$H_{my} = (E_{mp}^+ e^{-\gamma_m z \cos \phi_m} - E_{mp}^- e^{+\gamma_m z \cos \phi_m}) e^{-\gamma_m x \sin \phi_m} \sqrt{\epsilon_m} \sqrt{\epsilon_0 / \mu_0} \quad (2.4)$$

Writing $c_m = \sum_{i=1}^{m-1} d_i$, applying boundary conditions (tangential components of both electric and magnetic vectors be continuous at the boundary [6]) for the m^{th} surface separating the medium m and $m-1$, and then do the transformation, we can obtain

- For the **p** component

$$\begin{aligned} & E_{m-1,p}^+ e^{-\gamma_{m-1} c_m \cos \phi_{m-1}} \\ &= \frac{1}{2} \left(\frac{\cos \phi_m}{\cos \phi_{m-1}} + \frac{\sqrt{\epsilon_m}}{\sqrt{\epsilon_{m-1}}} \right) E_{m,p}^+ e^{-\gamma_m c_m \cos \phi_m} + \frac{1}{2} \left(\frac{\cos \phi_m}{\cos \phi_{m-1}} - \frac{\sqrt{\epsilon_m}}{\sqrt{\epsilon_{m-1}}} \right) E_{m,p}^- e^{+\gamma_m c_m \cos \phi_m} \\ &= \frac{1}{\tau_{m,p}} E_{m,p}^+ e^{-\gamma_m c_m \cos \phi_m} + \frac{\rho_{m,p}}{\tau_{m,p}} E_{m,p}^- e^{+\gamma_m c_m \cos \phi_m} \end{aligned} \quad (2.5)$$

$$\begin{aligned}
& E_{m-1,p}^- e^{+\gamma_{m-1} c_m \cos \phi_{m-1}} \\
&= \frac{1}{2} \left(\frac{\cos \phi_m}{\cos \phi_{m-1}} - \frac{\sqrt{\epsilon_m}}{\sqrt{\epsilon_{m-1}}} \right) E_{m,p}^+ e^{-\gamma_m c_m \cos \phi_m} + \frac{1}{2} \left(\frac{\cos \phi_m}{\cos \phi_{m-1}} + \frac{\sqrt{\epsilon_m}}{\sqrt{\epsilon_{m-1}}} \right) E_{m,p}^- e^{+\gamma_m c_m \cos \phi_m} \\
&= \frac{\rho_{m,p}}{\tau_{m,p}} E_{m,p}^+ e^{-\gamma_m c_m \cos \phi_m} + \frac{1}{\tau_{m,p}} E_{m,p}^- e^{+\gamma_m c_m \cos \phi_m}
\end{aligned} \tag{2.6}$$

where $\rho_{m,p}$ and $\tau_{m,p}$ are Fresnel coefficients for the parallel (**p**) polarization at the m^{th} surface (separating medium m-1 and m), given by

$$\rho_{m,p} = \frac{\sqrt{\epsilon_{m-1}} \cos \phi_m - \sqrt{\epsilon_m} \cos \phi_{m-1}}{\sqrt{\epsilon_{m-1}} \cos \phi_m + \sqrt{\epsilon_m} \cos \phi_{m-1}} \quad \tau_{m,p} = \frac{2\sqrt{\epsilon_{m-1}} \cos \phi_m}{\sqrt{\epsilon_{m-1}} \cos \phi_m + \sqrt{\epsilon_m} \cos \phi_{m-1}} \tag{2.7}$$

- For the **s** component

$$\begin{aligned}
& E_{m-1,s}^+ e^{-\gamma_{m-1} c_m \cos \phi_{m-1}} \\
&= \frac{1}{2} \left(1 + \frac{\sqrt{\epsilon_m} \cos \phi_m}{\sqrt{\epsilon_{m-1}} \cos \phi_{m-1}} \right) E_{m,s}^+ e^{-\gamma_m c_m \cos \phi_m} + \frac{1}{2} \left(1 - \frac{\sqrt{\epsilon_m} \cos \phi_m}{\sqrt{\epsilon_{m-1}} \cos \phi_{m-1}} \right) E_{m,s}^- e^{+\gamma_m c_m \cos \phi_m} \\
&= \frac{1}{\tau_{m,s}} E_{m,s}^+ e^{-\gamma_m c_m \cos \phi_m} + \frac{\rho_{m,s}}{\tau_{m,s}} E_{m,s}^- e^{+\gamma_m c_m \cos \phi_m}
\end{aligned} \tag{2.8}$$

$$\begin{aligned}
& E_{m-1,s}^- e^{+\gamma_{m-1} c_m \cos \phi_{m-1}} \\
&= \frac{1}{2} \left(1 - \frac{\sqrt{\epsilon_m} \cos \phi_m}{\sqrt{\epsilon_{m-1}} \cos \phi_{m-1}} \right) E_{m,s}^+ e^{-\gamma_m c_m \cos \phi_m} + \frac{1}{2} \left(1 + \frac{\sqrt{\epsilon_m} \cos \phi_m}{\sqrt{\epsilon_{m-1}} \cos \phi_{m-1}} \right) E_{m,s}^- e^{+\gamma_m c_m \cos \phi_m} \\
&= \frac{\rho_{m,s}}{\tau_{m,s}} E_{m,s}^+ e^{-\gamma_m c_m \cos \phi_m} + \frac{1}{\tau_{m,s}} E_{m,s}^- e^{+\gamma_m c_m \cos \phi_m}
\end{aligned} \tag{2.9}$$

where $\rho_{m,s}$ and $\tau_{m,s}$ are Fresnel coefficients for the perpendicular (**s**) polarization at the m^{th} surface (separating medium m-1 and m), given by

$$\rho_{m,s} = \frac{\sqrt{\epsilon_{m-1}} \cos \phi_{m-1} - \sqrt{\epsilon_m} \cos \phi_m}{\sqrt{\epsilon_{m-1}} \cos \phi_{m-1} + \sqrt{\epsilon_m} \cos \phi_m} \quad \tau_{m,s} = \frac{2\sqrt{\epsilon_{m-1}} \cos \phi_{m-1}}{\sqrt{\epsilon_{m-1}} \cos \phi_{m-1} + \sqrt{\epsilon_m} \cos \phi_m} \tag{2.10}$$

Comparing equation (2.5), (2.6) and equation (2.8), (2.9), we find the forms of the resulting equations for the **p** and **s** components are identical, thus the suffix p and s are dropped and the equations are given as below:

$$E_{m-1}^+ e^{-\gamma_{m-1} c_m \cos \phi_{m-1}} = (E_m^+ e^{-\gamma_m c_m \cos \phi_m} + \rho_m E_m^- e^{+\gamma_m c_m \cos \phi_m}) / \tau_m \tag{2.11}$$

$$E_{m-1}^- e^{+\gamma_{m-1} c_m \cos \phi_{m-1}} = (\rho_m E_m^+ e^{-\gamma_m c_m \cos \phi_m} + E_m^- e^{+\gamma_m c_m \cos \phi_m}) / \tau_m \tag{2.12}$$

Equation (2.11) and (2.12) can be written in a matrix form as

$$\begin{bmatrix} E_{m-1}^+ \\ E_{m-1}^- \end{bmatrix} = \frac{1}{\tau_m} \begin{bmatrix} e^{-c_m (\gamma_m \cos \phi_m - \gamma_{m-1} \cos \phi_{m-1})} & \rho_m e^{c_m (\gamma_m \cos \phi_m + \gamma_{m-1} \cos \phi_{m-1})} \\ \rho_m e^{-c_m (\gamma_m \cos \phi_m + \gamma_{m-1} \cos \phi_{m-1})} & e^{c_m (\gamma_m \cos \phi_m - \gamma_{m-1} \cos \phi_{m-1})} \end{bmatrix} \begin{bmatrix} E_m^+ \\ E_m^- \end{bmatrix} \tag{2.13}$$

For the stratified media of n layers locating in free space shown in Fig.2.1, we are interested in the relation between E_0^+ and E_{n+1}^+ , E_0^- and E_{n+1}^- . Since there is no negative-going wave in the $(n+1)^{th}$ medium, then $E_{n+1}^- = 0$. Thus from equation (2.13), we obtain

$$\begin{bmatrix} E_0^+ \\ E_0^- \end{bmatrix} = \frac{(C_1)(C_2)...(C_{n+1})}{(\tau_1)(\tau_2)...(\tau_{n+1})} \begin{bmatrix} E_{n+1}^+ \\ E_{n+1}^- = 0 \end{bmatrix} \quad (2.14)$$

where

$$(C_m) = \begin{bmatrix} e^{-c_m(\gamma_m \cos \phi_m - \gamma_{m-1} \cos \phi_{m-1})} & \rho_m e^{c_m(\gamma_m \cos \phi_m + \gamma_{m-1} \cos \phi_{m-1})} \\ \rho_m e^{-c_m(\gamma_m \cos \phi_m + \gamma_{m-1} \cos \phi_{m-1})} & e^{c_m(\gamma_m \cos \phi_m - \gamma_{m-1} \cos \phi_{m-1})} \end{bmatrix}$$

Writing the matrix product as

$$(C_1)(C_2)...(C_{n+1}) = \begin{bmatrix} a & b \\ c & d \end{bmatrix} \quad (2.15)$$

and from equation (2.14), the reflection and transmission coefficient of the stratified media can be given as

$$r = \frac{E_0^-}{E_0^+} = \frac{c}{a} \quad t = \frac{E_{n+1}^+}{E_0^+} = \frac{\tau_1 \tau_2 \dots \tau_{n+1}}{a} \quad (2.16)$$

Thus the reflectance and transmittance of the stratified media are given by

$$R = \frac{c}{a} \frac{c^*}{a^*} \quad T = \frac{\tau_1 \tau_2 \dots \tau_{n+1}}{a} \frac{\tau_1^* \tau_2^* \dots \tau_{n+1}^*}{a^*} \quad (2.17)$$

2.2. DIELECTRIC PROPERTIES OF THE PURE WATER

A review of the literature suggests that the most accurate model available at present for computing the dielectric constant of water is based on a double-Debye dielectric model (D3M) developed by William Ellison [7]. The D3M model is primarily developed for the seawater and it can be applied for pure water when the water salinity is set to zero.

The applicable range of conditions for the D3M is:

$$\begin{aligned} 0 &\leq T \leq 30^\circ\text{C} \\ 0 &\leq S \leq 40 \text{ psu} \\ 0 &\leq f \leq 1000 \text{ GHz} \end{aligned}$$

where T is the applicable temperature in $^\circ\text{C}$, f is the operational frequency in GHz and S is the water salinity in psu (practical salinity unit, with $1 \text{ psu} = 1(\text{‰})$). For pure water, $S = 0$. The real (ϵ'_w) and imaginary (ϵ''_w) part of the relative permittivity of water from D3M are given by

$$\epsilon'_w = \epsilon_{w\infty} + \frac{\epsilon_{w0} - \epsilon_{w1}}{1 + (2\pi f \tau_{w1})^2} + \frac{\epsilon_{w1} - \epsilon_{w\infty}}{1 + (2\pi f \tau_{w2})^2} \quad (2.18)$$

$$\epsilon''_w = \frac{2\pi f \tau_{w1}(\epsilon_{w0} - \epsilon_{w1})}{1 + (2\pi f \tau_{w1})^2} + \frac{2\pi f \tau_{w2}(\epsilon_{w1} - \epsilon_{w\infty})}{1 + (2\pi f \tau_{w2})^2} + \frac{\sigma_i}{2\pi \epsilon_0 f} \quad (2.19)$$

where ϵ_0 is the free space permittivity and σ_i refers to the ionic conductivity of the water solution when the solution contains dissolved salts. For pure water, $\sigma_i = 0$. The parameter functions in equation (2.18) and (2.19) are expressed by

$$\epsilon_{w0} = 87.85306 \exp\{-0.00456992T - a_1S - a_2S^2 - a_3ST\} \quad (2.20a)$$

$$\epsilon_{w1} = a_4 \exp\{-a_5T - a_6S - a_7ST\} \quad (2.20b)$$

$$\tau_{w1} = (a_8 + a_9S) \exp\{a_{10}/(T + a_{11})\} \text{ ns} \quad (2.20c)$$

$$\tau_{w2} = (a_{12} + a_{13}S) \exp\{a_{14}/(T + a_{15})\} \text{ ns} \quad (2.20d)$$

$$\epsilon_{w\infty} = a_{16} + a_{17}T + a_{18}S \quad (2.20e)$$

$$\sigma_i = \sigma(T, 35) \cdot P(S) \cdot Q(T, S) \quad (2.20f)$$

where

$$\sigma(T, 35) = 2.903602 + 8.607 \cdot 10^{-2}T + 4.738817 \cdot 10^{-4}T^2 - 2.991 \cdot 10^{-6}T^3 + 4.3041 \cdot 10^{-9}T^4 \quad (2.21a)$$

$$P(S) = S \frac{37.5109 + 5.45216S + 0.014409S^2}{1004.75 + 182.283S + S^2} \quad (2.21b)$$

$$Q(T, S) = 1 + \alpha_0(T - 15)/(T + \alpha_1) \quad (2.21c)$$

$$\alpha_0 = \frac{6.9431 + 3.2841S - 0.099486S^2}{84.85 + 69.024S + S^2} \quad (2.21d)$$

$$\alpha_1 = 49.843 - 0.2276S + 0.00198S^2 \quad (2.21e)$$

The other coefficients a_1 to a_{18} in equation (2.20) are listed in Table 2.1.

Table 2.1: Values of coefficients in equation (2.20) of D3M

	Values of coefficients of D3M		Values of coefficients of D3M
a_1	0.46606917E-02	a_{10}	0.58366888E+03
a_2	-0.26087876E-04	a_{11}	0.12684992E+03
a_3	-0.63926782E-05	a_{12}	0.69227972E-04
a_4	0.63000075E+01	a_{13}	0.38957681E-06
a_5	0.26242021E-02	a_{14}	0.30742330E+03
a_6	-0.42984155E-02	a_{15}	0.12634992E+03
a_7	0.34414691E-04	a_{16}	0.37245044E+01
a_8	0.17667420E-03	a_{17}	0.92609781E-02
a_9	-0.20491560E-06	a_{18}	-0.26093754E-01

According to William Ellison, the accuracy of estimated dielectric constant of pure water based on D3M is within 1%, 3% and 5% at the frequency range of 0~20GHz, 30~100GHz and 100~1000GHz respectively. If the temperature T is set to be 20°C, then the real part (ϵ') of relative permittivity, imaginary part (dielectric loss factor ϵ'') of relative permittivity and the loss tangent (ϵ'/ϵ'') of pure water over 0~200GHz from D3M are shown in Fig.2.2.

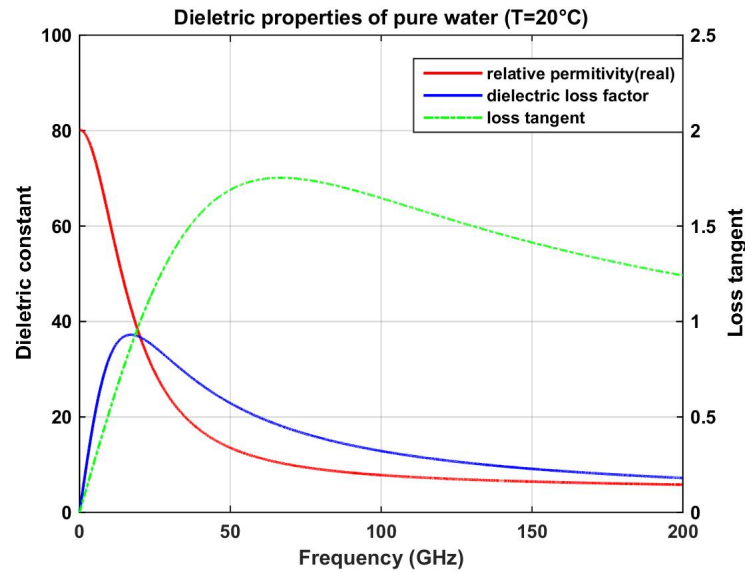


Figure 2.2: Dielectric constant of pure water versus frequency estimated from the double-Debye dielectric model ($T=20^{\circ}\text{C}$)

From Figure 2.2, it can be seen at 20°C , the real part ϵ' of relative permittivity of pure water decreases with the frequency. As to the dielectric loss factor ϵ'' of pure water, it gradually reaches the maximum at the first relaxation frequency $f_1 = 1/(2\pi\tau_{w1}) = 16.93\text{GHz}$, and then starts to decrease with the frequency smoothly. Additionally, the loss tangent of pure water reaches its maximum at the frequency around 64GHz which implies the strongest energy absorption of water at this frequency.

The temperature dependency (-20°C - 50°C) of the dielectric constant of pure water at 77GHz is given in Fig.2.3. From this graph, it is observed that both the real relative permittivity ϵ' and dielectric loss factor ϵ'' of the pure water increases with the temperature. As to the loss tangent, it reaches the maximum at the temperature around 25°C (room temperature) which implies the highest energy absorption of pure water.

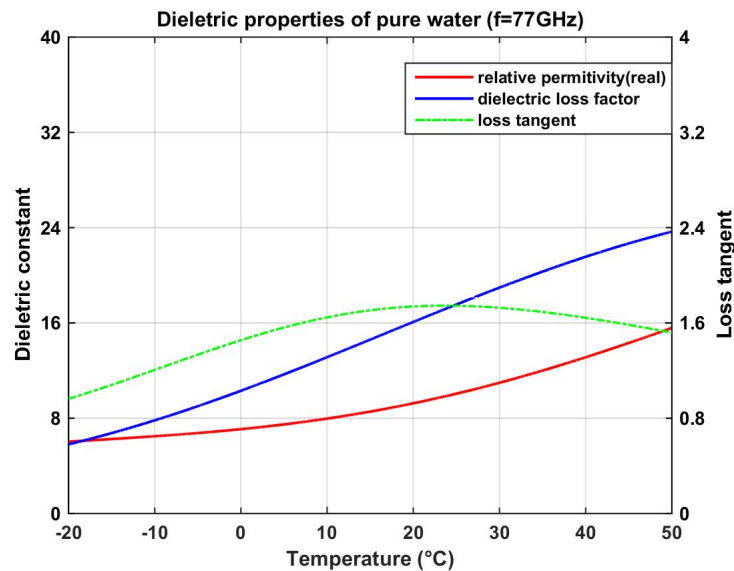


Figure 2.3: Dielectric constant of pure water versus temperature estimated from the double-Debye dielectric model ($f=77\text{GHz}$)

2.3. REFLECTANCE AND TRANSMITTANCE OF THE SINGLE PURE WATER FILM

According to section 2.1, the wave reflection and transmission coefficient of a single film are given by

$$r = \frac{\rho_1 e^{\gamma_1 d_1 \cos \phi_1} + \rho_2 e^{-\gamma_1 d_1 \cos \phi_1}}{e^{\gamma_1 d_1 \cos \phi_1} + \rho_1 \rho_2 e^{-\gamma_1 d_1 \cos \phi_1}} \quad (2.22)$$

$$t = \frac{\tau_1 \tau_2 e^{\gamma_2 d_1 \cos \phi_2}}{e^{\gamma_1 d_1 \cos \phi_1} + \rho_1 \rho_2 e^{-\gamma_1 d_1 \cos \phi_1}} \quad (2.23)$$

where ρ_1 , τ_1 and ρ_2 , τ_2 are Fresnel coefficients at the surface separating the air and the medium and surface separating the medium and air respectively, ϕ_1 and ϕ_2 are the incident angles in the medium film and air respectively, γ_1 and γ_2 are the wave propagation constant in the medium and air respectively and d_1 [m] is the thickness of the medium film. Substituting the water dielectric constant estimated from the double-Debye dielectric model (shown in Fig.2.2) into equation (2.22) and (2.23) and the reflectance and transmittance of a single water film versus thicknesses with normal incidence can be obtained shown in Fig.2.4 and Fig.2.5 respectively.

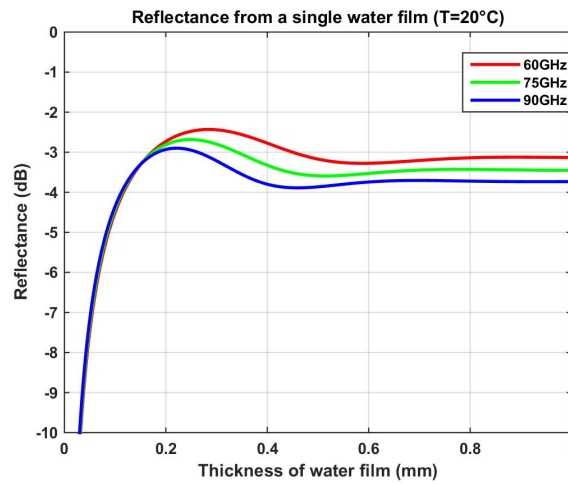


Figure 2.4: Reflectance from the single water film versus thickness (T=20°C, normal incidence)

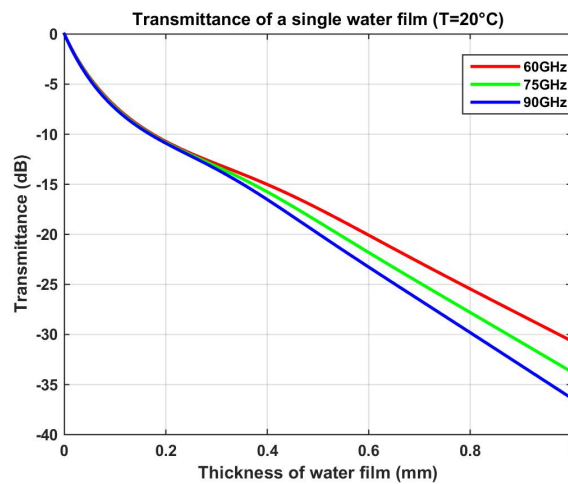


Figure 2.5: Transmittance of the single water film versus thickness (T=20°C, normal incidence)

From Fig.2.4, it is observed that when the operational frequency is 60GHz, 75GHz and 90GHz respectively, the reflectance from the single water film with normal incidence does not change much with the frequency, less than 1 dB variation. With the increasing thickness of the water film, the reflectance for each specific frequency tends to be constant due to the limited wave penetration in the water.

From Fig.2.5, it can be seen that for normal incidence at 20°C, when the thickness of water film is less than 0.3mm, the transmittance of a single water film at 60GHz, 75GHz and 90GHz is almost the same. When the thickness of water film continues to increase, the transmittance decreases with the increasing frequency. If the thickness of water film is larger than 0.5mm, the transmittance will be less than -20dB. Thus the existence of water film can dramatically shorten the maximum radar detection range.

2.4. CONCLUSIONS

In this chapter, the computation of reflectance and transmittance of the stratified lossy media is achieved by applying the propagation matrix approach (PMA). The basic idea of PMA is to relate the electric fields and magnetic fields in two adjacent layers by using the boundary conditions and it is applicable with the plane wave assumption.

A double-Debye dielectric model (D3M) is introduced to estimate the dielectric properties of pure water. At 20°C, the real part of relative permittivity of pure water ϵ' decreases with the frequency. While for the dielectric loss factor of pure water ϵ'' , it gradually reaches the maximum at the first relaxation frequency (16.93GHz), and then starts to decrease with the frequency smoothly and the maximum energy absorption occurs at the frequency about 64GHz. As to the temperature dependency of the water dielectric permittivity at 77GHz, both the real relative permittivity ϵ' and dielectric loss factor ϵ'' of pure water increases with the temperature and the maximum energy absorption of water occurs at the temperature around 25°C.

The water film attenuates the electromagnetic power significantly. If the radar operates at 60GHz, 75GHz or 90GHz at the temperature of 20°C, only 1% power can be transmitted when a water film with 0.5-0.6mm thickness is formed on the surface of radar and it implies that the existence of water film on the surface of the radar can severely decrease the maximum radar detection range.

3

THEORETICAL AND EXPERIMENTAL MODELS FOR WAVE PROPAGATION ON WET RADOMES

In this chapter, primarily the theoretical model of wave propagation on the radome covered with various thicknesses of the water film over the whole automotive frequency band from 75GHz to 85GHz is derived and analysed. According to the theoretical findings, an appropriate lab measurement system is applied to experimentally investigate the water film effects on the wave propagation through the radome. And then based on the results of real measurements, the experimental model can be obtained. Finally, comparisons between these two models are discussed and analysed.

3.1. DERIVATION OF THE THEORETICAL MODEL FOR WAVE PROPAGATION ON THE WET RADOME

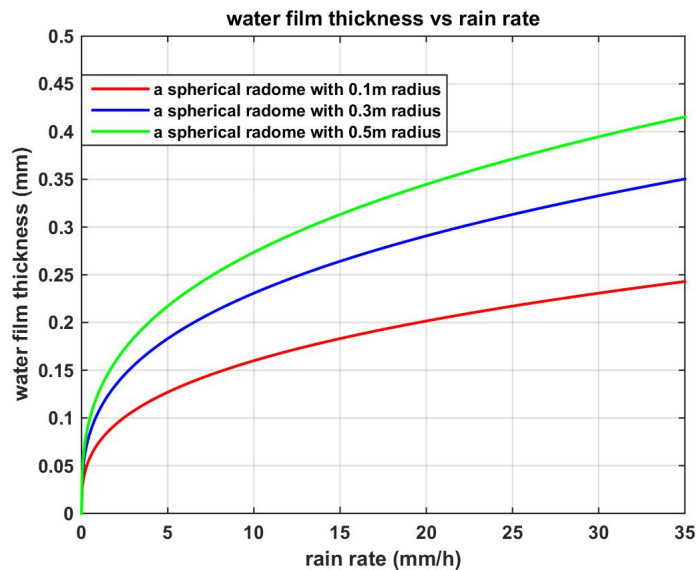


Figure 3.1: The formed thickness of the water film for a spherical radome with 0.1m/0.3m/0.5m radius versus rain rate

During adverse weather, a thin water film can be easily formed on the surface of radome. Fig.3.1 shows the relation between the rain rate and the corresponding formed thickness of the water film on the surface of a spherical radome with 0.1m, 0.3m or 0.5m radius which is derived from Gibble's formula [8]. Then practically if the rain rate (mm/h) is known during the adverse weather, the formed thickness of water film on the surface of the automotive radar can be estimated. Thus our work is focused on the investigation of uniform water film effects on the wave propagation on the radome. The propagation of radar signals on such a multilayer structure (air-radome-water) can be represented by the model shown in Fig.3.2.

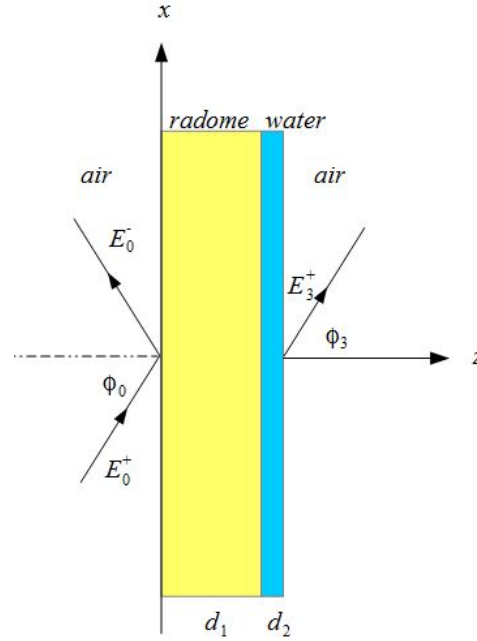


Figure 3.2: The theoretical model of wave propagation on the wet radome

By applying propagation matrix approach described in chapter 2, the calculated reflection and transmission coefficients of this radome-water system are given as:

$$r = \frac{\rho_1 + \rho_2 e^{-2\gamma_1 d_1 \cos \phi_1} + \rho_3 e^{-2(\gamma_1 d_1 \cos \phi_1 + \gamma_2 d_2 \cos \phi_2)} + \rho_1 \rho_2 \rho_3 e^{-2\gamma_2 d_2 \cos \phi_2}}{1 + \rho_1 \rho_2 e^{-2\gamma_1 d_1 \cos \phi_1} + \rho_1 \rho_3 e^{-2(\gamma_1 d_1 \cos \phi_1 + \gamma_2 d_2 \cos \phi_2)} + \rho_2 \rho_3 e^{-2\gamma_2 d_2 \cos \phi_2}} \quad (3.1)$$

$$t = \frac{\tau_1 \tau_2 \tau_3 e^{-\gamma_1 d_1 \cos \phi_1} e^{-\gamma_2 d_2 \cos \phi_2} e^{\gamma_3 (d_1 + d_2) \cos \phi_3}}{1 + \rho_1 \rho_2 e^{-2\gamma_1 d_1 \cos \phi_1} + \rho_1 \rho_3 e^{-2(\gamma_1 d_1 \cos \phi_1 + \gamma_2 d_2 \cos \phi_2)} + \rho_2 \rho_3 e^{-2\gamma_2 d_2 \cos \phi_2}} \quad (3.2)$$

where:

ρ_1, ρ_2, ρ_3 : Reflection coefficient at the surface separating the air-radome, radome-water and water-air;

τ_1, τ_2, τ_3 : Transmission coefficient between the adjacent media;

$\gamma_1, \gamma_2, \gamma_3$: Propagation constant in the radome, water and air respectively;

ϕ_1, ϕ_2, ϕ_3 : Refractive angle in the radome, water and air respectively.

d_1, d_2 : Thickness of the radome and water film [m];

For the wave propagation model in Fig.3.2, if we assume the dielectric constant of the radome (yellow) is 2.678-0.027j, the thickness of the radome $d_1 = 4.01 \text{ mm}$ and the incident angle $\phi_0 = 0^\circ$, varying the thickness of water film d_2 from 0.085mm to 0.51mm with 0.085mm per step, then by applying equation (3.1) and (3.2), the calculated reflectance and transmittance of the radome covered with various thicknesses of water film over the whole automotive frequency band at 17.5°C are shown in Fig.3.3 and Fig.3.4 respectively.

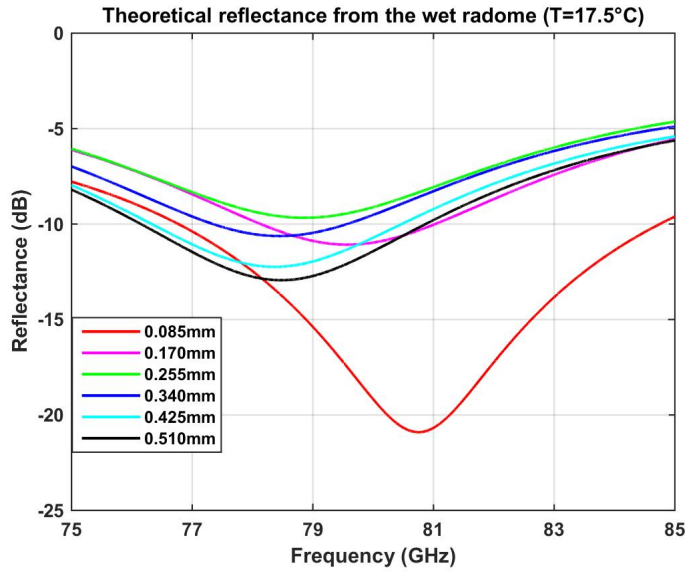


Figure 3.3: Theoretical reflectance from the backside of the radome covered with various thicknesses of the water film

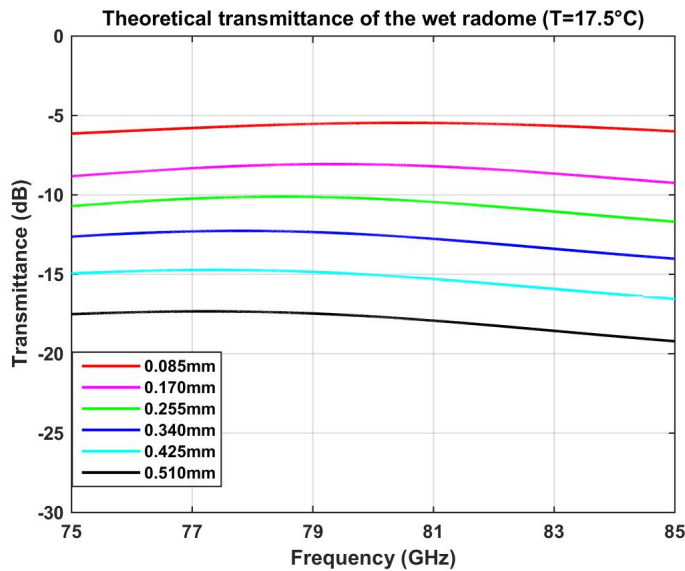


Figure 3.4: Theoretical transmittance of the radome covered with various thicknesses of the water film

Fig.3.3 describes the theoretical reflectance from the backside of the radome covered by various thicknesses of water film from 75GHz to 85GHz. It is observed that for each specific thickness of water film, there is a corresponding resonant frequency where the minimum reflectance from the backside of the wet radome occurs over the whole bandwidth and it is shown in Table.3.1.

Table 3.1: Comparisons of theoretical reflectance from the backside of the radome covered with various thicknesses of water film

	0.085mm	0.170mm	0.255mm	0.340mm	0.425mm	0.510mm
MR (dB)	-20.90	-11.08	-9.67	-10.63	-12.24	-12.94
RF (GHz)	80.75	79.55	78.85	78.46	78.41	78.40

Note: **MR** : minimum reflectance; **RF**: resonant frequency;

From Table.3.1, it is observed that the resonant frequency of the reflectance decreases when the thickness of water film is increased. When the thickness of water film increases from 0.085mm to 0.170mm, the resonant frequency significantly shifts from 80.75GHz to 79.55GHz. While when the thickness continues to increase from 0.255m to 0.510mm, the variation of resonant frequency is less than 0.5GHz. Thus the resonant frequency of reflectance is more sensitive to the thinner water film. In addition, comparing the reflectance frequency response curves in Fig.3.3, it can be seen that when the water film is thin, the reflectance frequency response curve of the wet radome is significantly different from the ones when the water film is thick.

These two phenomena are caused by the same reasons. When the water film is thin, still a large portion of the power will be reflected back from the surface separating the water and air which will interfere with the reflected power from the surface separating the air and radome. Since this interference is related to the propagation path, thus both the resonant frequency and reflectance frequency response will be sensitive to the thickness of water film. While when the thickness of water film is large, the wave propagating on the water film suffers relatively high power absorption and then the power reflected from the surface separating the water and air will be small. Due to the limited power penetration in the water, reflectance from the wet radome will become converged with the increase of the thickness of water film.

Fig.3.4 shows the theoretical transmittance of the radome covered by various thicknesses of water film from 75Gz to 85GHz. For each specific thickness of water film, the transmittance of the wet radome slightly increase with the frequency, reaching the maximum, then starting to decrease gradually with the frequency. For each specific frequency, the transmittance of the wet radome decreases about 2~3dB per step when the thickness of the water film increases from 0.085mm to 0.51mm with 0.085mm per step. The calculated transmittance of the radome covered with various thicknesses of water film at 75GHz and 85GHz are shown in Table 3.2.

Table 3.2: Comparisons of calculated transmittance of the radome covered with various thicknesses of water film

	0.085mm	0.170mm	0.255mm	0.340mm	0.425mm	0.510mm
75 (GHz)	-6.13dB	-8.82dB	-10.69dB	-12.62dB	-14.94dB	-17.51dB
85 (GHz)	-6.00dB	-9.24dB	-11.68dB	-14.01dB	-16.53dB	-19.22dB

3.2. DERIVATION OF THE EXPERIMENTAL MODEL FOR WAVE PROPAGATION ON THE WET RADOME

In section 3.1, the theoretical model of wave propagation on the wet radome covered with various thicknesses of water film is derived. Now extensive real measurements on the reflectance and transmittance of the wet radome are performed in order to validate the theoretical model.

3.2.1. EXPERIMENTAL SETTINGS FOR MEASUREMENTS OF WAVE PROPAGATION ON THE WET RADOME

Fig.3.5 shows the experimental settings for the real measurements of wave propagation on the wet radome. The Vector Network Analyser (N5260-60003, VNA) operating from 67GHz to 110GHz is used to perform all the measurements. Two w-band (73.8~112GHz) pyramid horn antennas with approximate 22° 3-dB beam width are used as a transmitter and a receiver respectively. Normally the instrument measures the S-parameters and displays the results in the frequency domain.

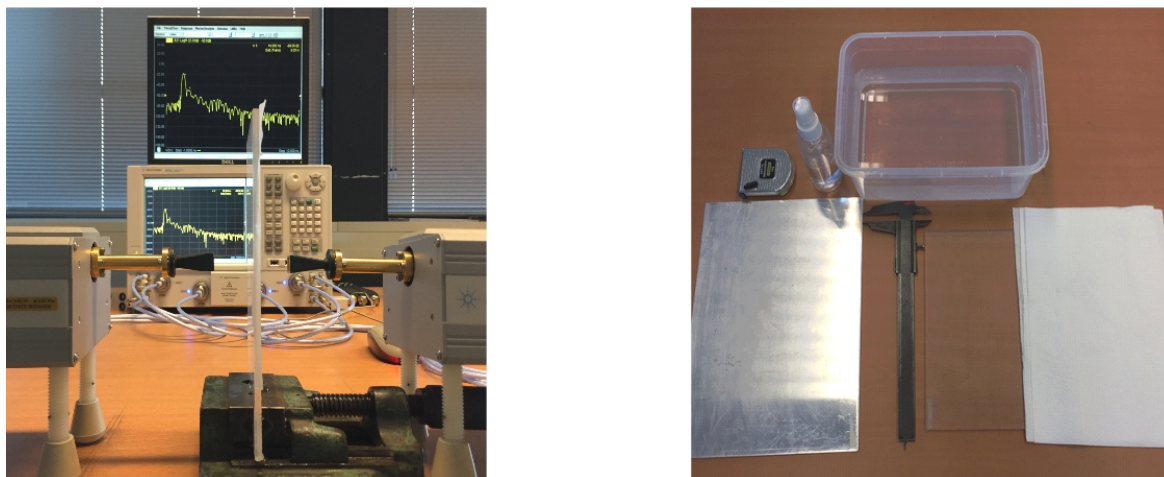


Figure 3.5: Experimental settings for the measurements of wave propagation on the wet radome

- Operational frequency of the network analyser: 75GHz~85GHz.
- Temperature: $17.5^{\circ}\text{C} \pm 0.5^{\circ}\text{C}$.
- Properties of the radome

The experimental radome with a size of $185\text{mm} \times 100\text{mm} \times 4.01\text{mm}$ is located in the middle of two antennas. Ideally it should be horizontally aligned in order to easily form a uniform water film on the surface of the radome. However, it is difficult to rotate the orientation of the antennas to be vertical considering our experimental conditions. Thus the radome is vertically aligned shown in Fig.3.5.

Primarily, the relative permittivity of the radome was unknown. Some measurements described in appendix A were performed to determine this value and it was found that the measured dielectric constant of the radome $\epsilon = 2.678 - 0.027j$. Thus both the radome thickness and the dielectric constant of the radome are consistent with the properties of the radome used for the theoretical model.

- Calibration of the free space propagation loss

Since we are only interested in the reflectance from the surface of the radome, and the reflectance measured by VNA suffers from the free space propagation loss. Thus specific calibration steps are required. For the reflectance, a perfect flat metal plate is used to perform the calibration steps. According to the boundary conditions, all the power will be reflected back from a perfect metal plate. Thus for each measurement, primarily reflectance from the flat metal plate R_m is measured. And then in the same reference position, reflectance from the wet radome R_r is measured. Thus the ratio $R = R_r / R_m$ is the actual reflectance from the backside surface of the wet radome after removing the propagation loss.

In the same way, as to the calibration of free space propagation loss for transmittance, primarily the free space transmittance between two antennas T_f is measured. And then the transmittance through the wet radome T_r is measured. Thus the ratio $T = T_r / T_f$ is the interested actual transmittance of the wet radome after removing the propagation loss.

- Tissue papers used as the water carrier

The tissue paper is selected as a proper water carrier basically for its two properties: For one thing, the tissue papers own a relatively high water absorption capacity without dissolving. For another, the dielectric of the tissue papers has a quite small real permittivity and negligible loss factor at millimetre wave frequencies compared to the dielectric permittivity of water [9]. Thus the effects of tissue paper on the experiments are insignificant.

- Application of the spray

Since the wet tissue paper is vertically mounted on the surface of the radome, the water will drop down eventually due to the gravity. Thus the spray is used as the water supplement during the measurements which helps to keep the experimental accuracy.

Though the tissue paper is an ideal material as the water carrier, it is difficult to keep the wetness grade constant during the measurements due to gravity. Additionally, the possible air gaps between wet tissues may further increase the experimental inaccuracy. Thus all the measurements are independently repeated 20 times and the averaged results will be calculated in order to suppress these effects.

As to the determination of the thickness of water film, the calliper with 0.005mm accuracy is used to measure the total thickness of 20 layers of wet tissue papers. The measured mean thickness of a single layer of wet tissue paper is about 0.085mm and we take this value as the thickness of a single water film. Thus thickness of the water film covered on the radome can be increased by overlapping the wet tissue papers during the measurements.

3.2.2. EXPERIMENTAL RESULTS OF REFLECTANCE FROM THE BACKSIDE OF THE WET RADOME

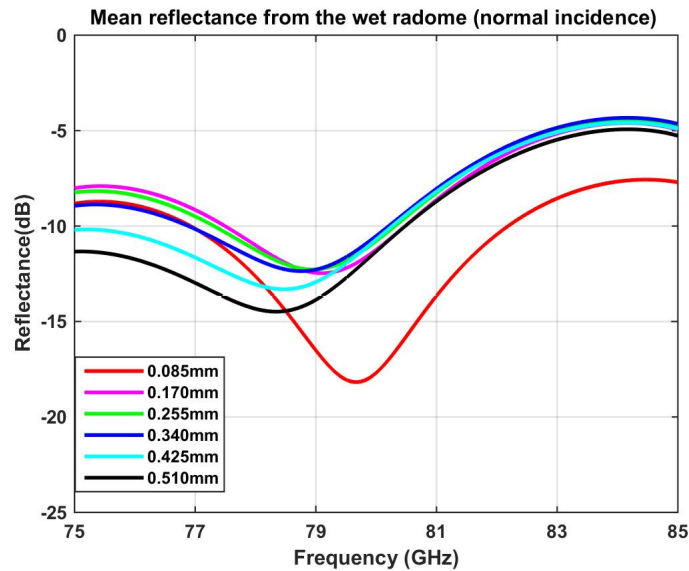


Figure 3.6: Measured mean reflectance from the backside of radome covered with various thicknesses of the water film

Fig.3.6 shows the measured mean reflectance from the backside of radome covered with various thicknesses of the water film over the whole frequency band (75GHz ~85GHz). For the reflectance from the radome covered with each specific thickness of the water film, it primarily decreases with the frequency, reaching the minimum at the resonant frequency, and then starts to increase with the frequency. When the thickness of water film increases from 0.085mm to 0.170mm, the variation of the reflectance frequency response curve is quite significant. While if the thickness of water film increases from 0.017mm until 0.510mm with 0.085mm per step, the variation of the reflectance frequency response curve is not as large as the thinner water film case. This phenomenon is caused by the same reasons as we discussed in section 3.1.

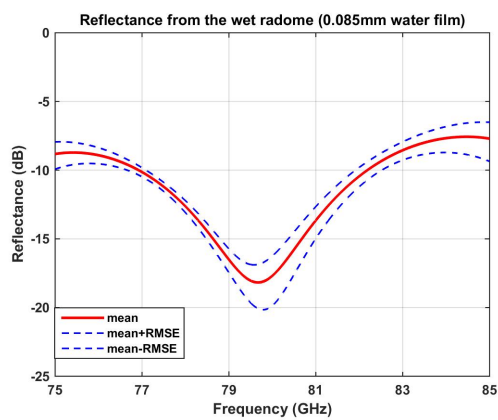
The reflectance at the resonant frequency for each specific thickness is shown in Table 3.3 and it is observed that the resonant frequency shifts to a lower frequency with the increasing thickness of water film.

Table 3.3: Comparisons of measured mean reflectance from the backside of radome covered with various thicknesses of water film

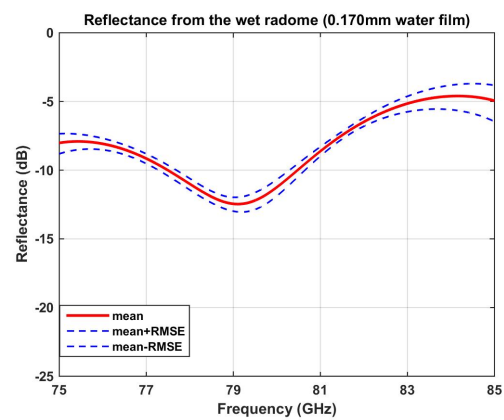
	0.085mm	0.170mm	0.255mm	0.340mm	0.425mm	0.510mm
MR (dB)	-18.18	-12.47	-12.28	-12.36	-13.31	-14.48
RF (GHz)	79.66	79.11	78.93	78.82	78.43	78.38

Note: **MR** : minimum reflectance; **RF**: resonant frequency;

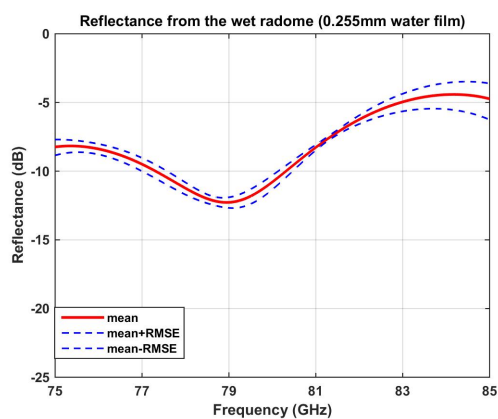
Since the accuracy of the measurements of the reflectance from the backside of wet radome is determined by many factors (imperfect calibration, imperfect orientation alignment of the radome, inconstant wetness grade, etc.), the root mean squared error (RMSE) among 20 independent measurements is calculated for each case and the corresponding error bar graph is shown in the Fig 3.7 (a)-(f).



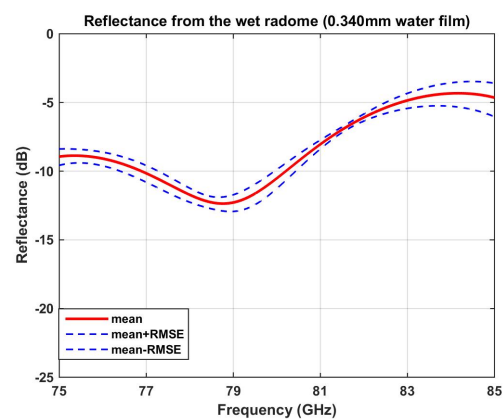
(a) 0.085mm



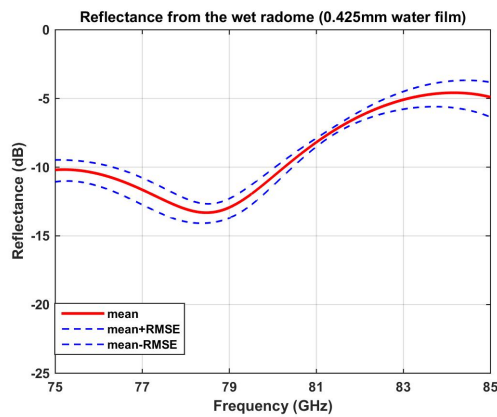
(b) 0.170mm



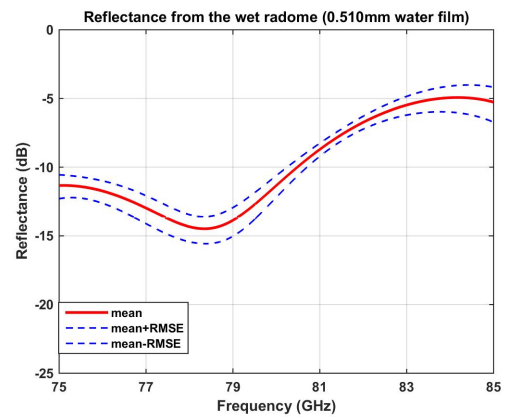
(c) 0.255mm



(d) 0.340mm



(e) 0.425mm

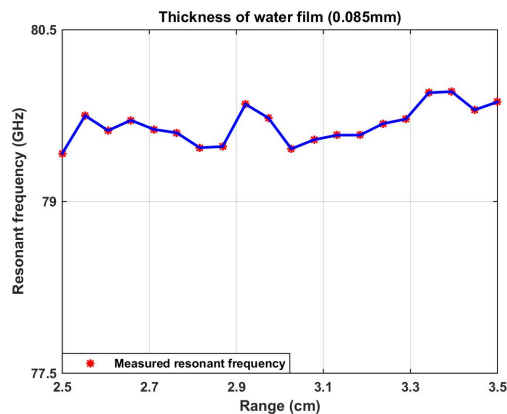


(f) 0.510mm

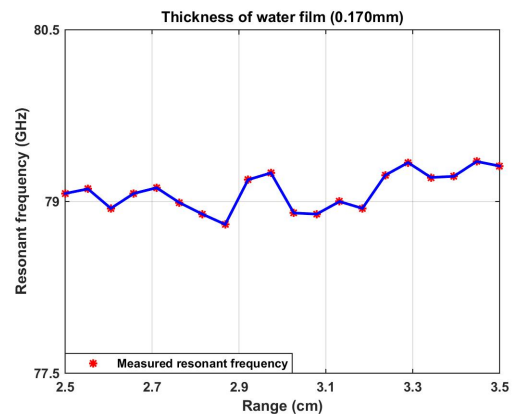
Figure 3.7: Error bar graphs for the reflectance from the backside of the wet radome among 20 measurements

From Fig.3.7, it is observed that when the water thickness is 0.085mm, the variance of measured reflectance around the resonant frequency is maximum compared to the variance of the measured reflectance for other thickness of the water film. This is because when the water thickness of the water film equals to 0.085mm, only a single wet tissue is mounted on the surface of the radome which suffers from the inconstant water distribution due to gravity more severely compared to the case with multi-layer tissue papers. For other measurements, generally the variance of measured reflectance along the whole frequency band is acceptable, less than 1dB.

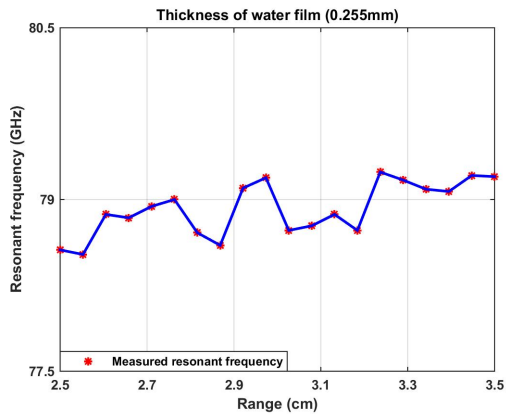
The resonant frequency where the minimum reflectance occurs is an important factor for the optimal radome/bumper design. Among 20 independent measurements for each case, the distance between the radome and antenna is tuned increasingly from 2.5cm to 3.5 cm. Then the measured resonant frequency corresponding to each specific range is shown in Fig.3.8 (a)-(f).



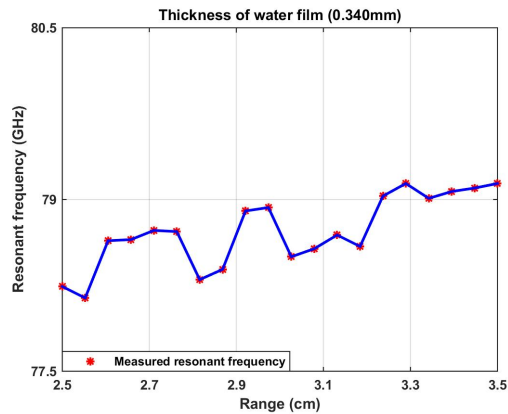
(a) 0.085mm



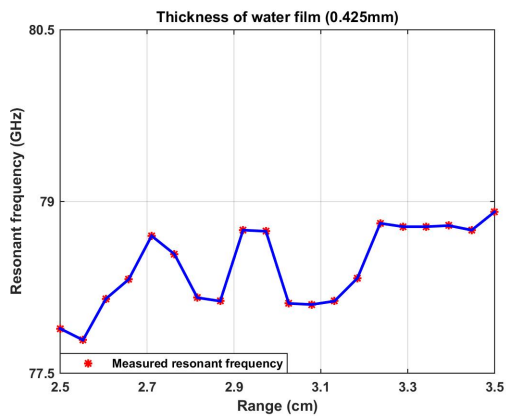
(b) 0.170mm



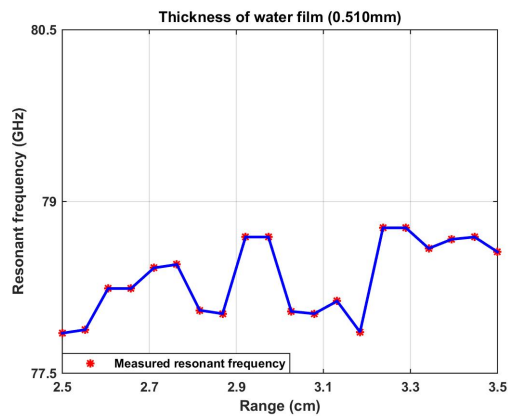
(c) 0.255mm



(d) 0.340mm



(e) 0.425mm



(f) 0.510mm

Figure 3.8: Variations of measured resonant frequencies of the reflectance from the backside of wet radome among 20 measurements

From Fig.3.8, it can be observed in each graph that when the range between the antenna and radome is tuned increasingly from 2.5cm to 3.5cm among 20 independent measurements, the resonant frequency of the reflectance from the backside of wet radome generally oscillates within an extent less than 1GHz. Comparing the six graphs above, it can be seen that the resonant frequency of reflectance oscillates with the range between the radome and antenna in a similar trend, regardless of the thickness of water film. Since the distance between the antenna and radome is only about 3cm during the measurements, not meeting the far field criterion $2D^2/\lambda$ [10] in the automotive frequency band, and thus these phenomena can be caused by the near-field spherical wave effects.

3.2.3. EXPERIMENTAL RESULTS OF THE TRANSMITTANCE OF THE WET RADOME

In the same way as the reflectance, the measurement of transmittance of the radome covered with the water film is independently repeated 20 times for each case and the mean transmittance of the wet radome is calculated shown in Fig.3.9.

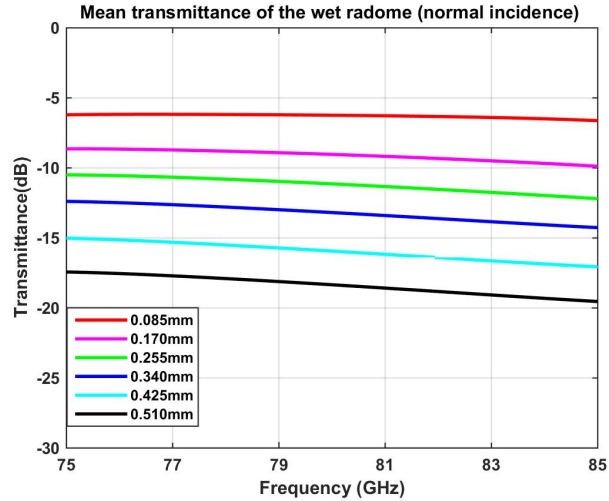


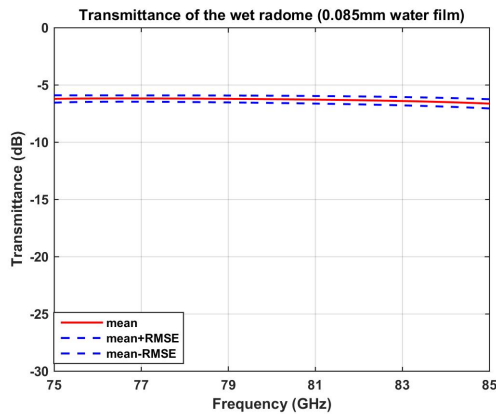
Figure 3.9: Measured mean transmittance of the radome covered with various thicknesses of the water film

Fig.3.9 shows the measured mean transmittance ($T=17.5^{\circ}\text{C}\pm 0.5^{\circ}\text{C}$) of the radome covered with various thicknesses of the water film among 20 independent measurements over the whole automotive frequency band (75GHz~85GHz). For each specific thickness of the water film, the transmittance of the wet radome decreases with the increasing frequency. For each specific frequency, when the thickness of water film on the radome surface increases from 0.085mm to 0.51mm with 0.085mm per step, the transmittance of the wet radome decreases about 2~3 dB per step. The mean transmittance of the radome covered with various thicknesses of water film at 75GHz and 85GHz are shown in Table 3.4.

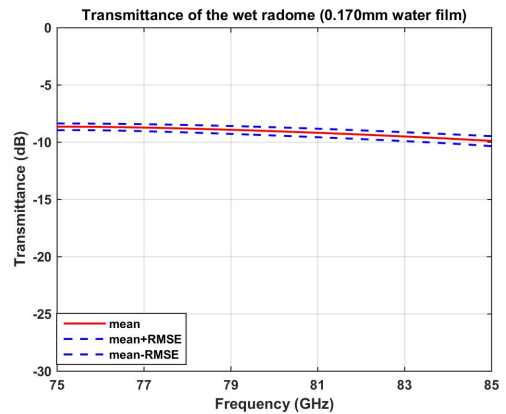
Table 3.4: Comparisons of measured mean transmittance of the radome covered with various thicknesses of water film

	0.085mm	0.170mm	0.255mm	0.340mm	0.425mm	0.510mm
75 (GHz)	-6.20dB	-8.64dB	-10.50dB	-12.39dB	-15.02dB	-17.43dB
85 (GHz)	-6.61dB	-9.86dB	-12.16dB	-14.24dB	-17.06dB	-19.51dB

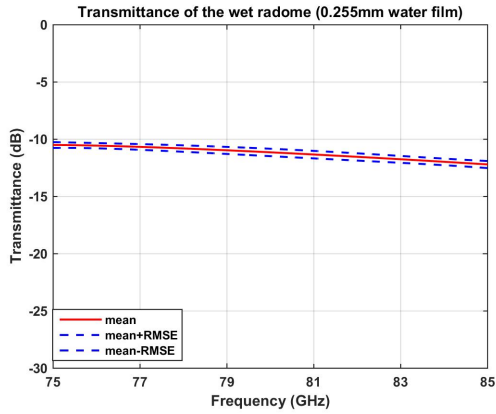
The root mean squared error (RMSE) for the transmittance of the wet radome among 20 independent measurements is calculated for each case and the corresponding error bar graph is shown in Fig.3.10 (a)-(f).



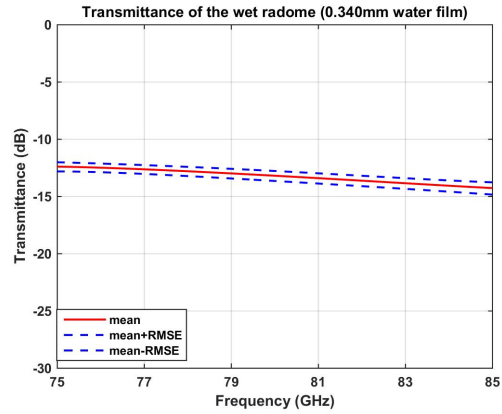
(a) 0.085mm



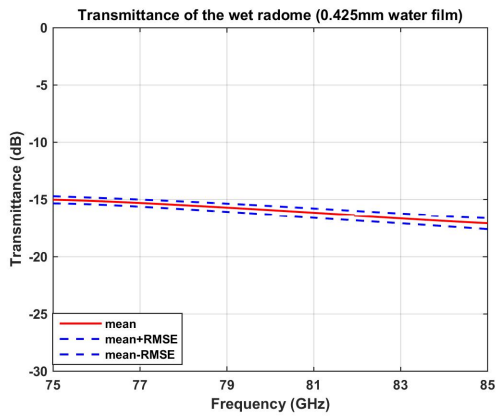
(b) 0.170mm



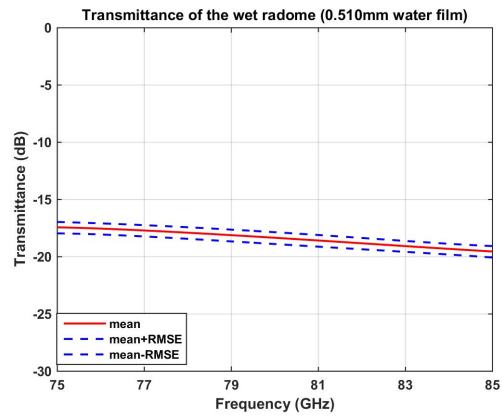
(c) 0.255mm



(d) 0.340mm



(e) 0.425mm



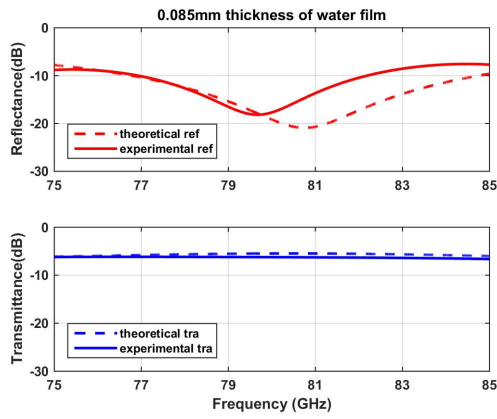
(f) 0.510mm

Figure 3.10: Error bar graphs for the transmittance of the wet radome among 20 measurements

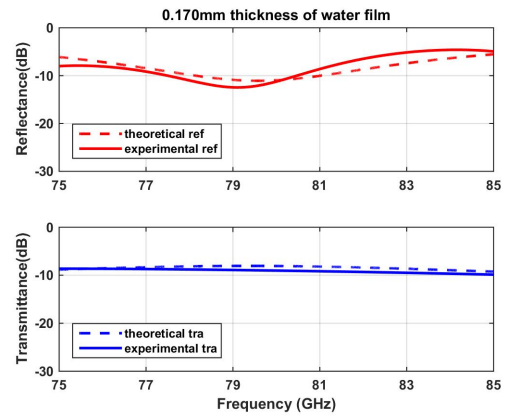
From Fig.3.10, it is observed that the variance of measured transmittance of the radome covered by each specific thickness of the water film in each graph is around 0~0.5dB, less than the general variance of measured reflectance of the wet radome in Fig.3.7. It is because the calibration of free space propagation loss for the transmittance is much stable compared to the calibration for the reflectance which is pretty sensitive to the orientation alignment of the metal plate. Thus the variance of measured reflectance will be larger than the variance of measured transmittance.

3.3. COMPARISONS OF THE EXPERIMENTAL AND THEORETICAL MODELS

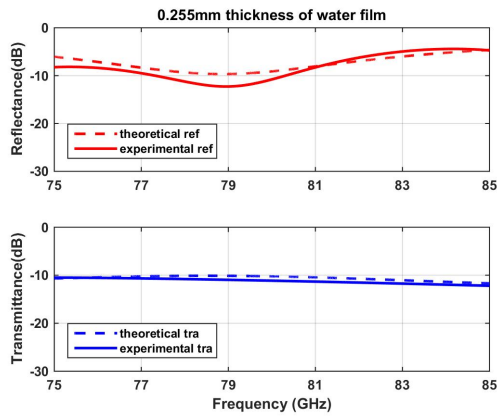
Fig.3.11 (a)-(f) shows the comparisons between theoretical and experimental models for the wave propagation on the radome covered with various thicknesses of water film. It is observed that for the transmittance of the wet radome, the experimental results are almost consistent with the theoretical expectations.



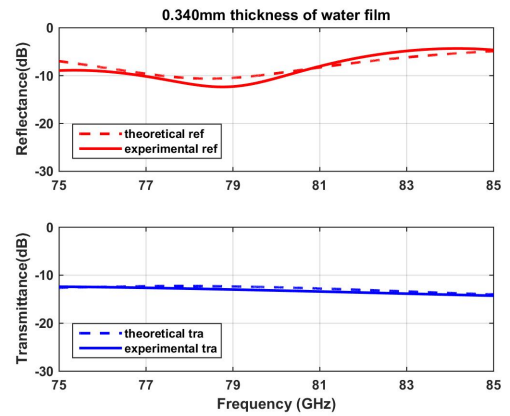
(a) 0.085mm



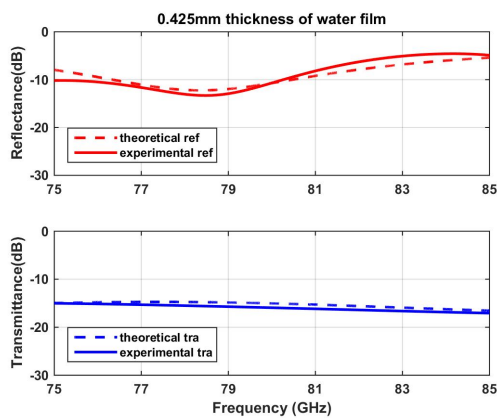
(b) 0.170mm



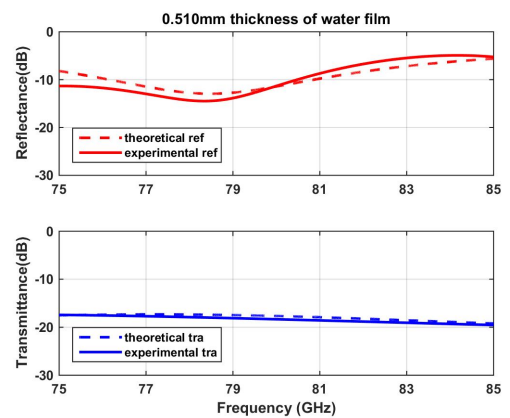
(c) 0.255mm



(d) 0.340mm



(e) 0.425mm



(f) 0.510mm

Figure 3.11: Comparisons between theoretical and experimental reflectance/transmittance of the wet radome

As to the reflectance from the backside of wet radome, the experimental reflectance is roughly matched to the theoretical results except for the case when the radome is covered with 0.085mm thickness of water film. As we already discussed before that when the water film is quite thin, the reflectance is quite sensitive to the thickness of water film. And during the measurement of the wave propagation on the single wet tissue paper (0.085mm) mounted on the surface of the radome, we found it suffered more severely from the inconstant water grade due to the gravity compared to the case when the radome was covered with multiple layers of the wet tissue papers. Thus the big bias between the experimental and theoretical reflectance of the radome covered with 0.085mm thickness of water film may be caused by the inaccurately estimated thickness of the water film. Then we tune the thickness of the water film for this case in the theoretical model and find that when the estimated thickness of the water film is changed from 0.085mm to 0.095mm, the experimental results generally follows the theoretical results shown in Fig.3.12.

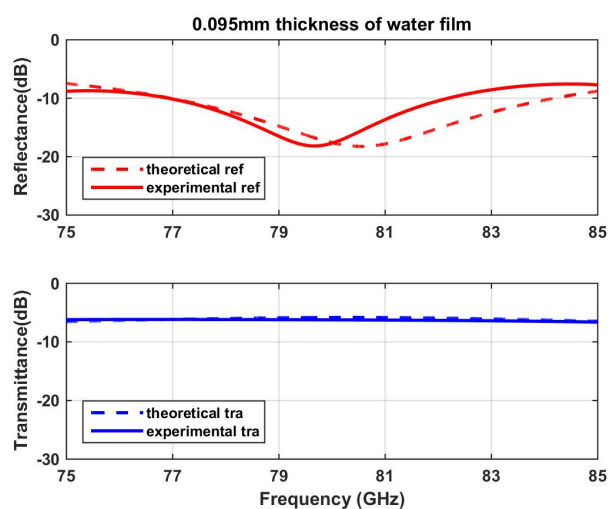


Figure 3.12: Theoretical and experimental reflectance and transmittance of the radome covered with 0.095mm thickness of water film

3.4. CONCLUSIONS

In this chapter, primarily the theoretical model ($T=17.5^{\circ}\text{C}$) of wave propagation on the radome covered with various thicknesses of water film is derived based on plane wave assumptions. From this model, for the reflectance from the backside of wet radome, it is observed that for each specific thickness of water film covered on the surface of radome, there is a corresponding resonant frequency where the minimum reflectance occurs over the whole automotive frequency band (75GHz~85GHz). This resonant frequency shifts to a lower frequency band with the increasing thickness of water film. Furthermore, when the water film is thin, the reflectance frequency response curve is quite sensitive to the thickness of water film. When the thickness of water film is larger than 0.255mm, the reflectance frequency response curve is becoming converged with the increasing thickness of water film.

As to the transmittance of the wet radome from the theoretical model, for each specific thickness of water film, the transmittance of the wet radome slightly increase with the frequency, reaching the maximum, and then starting to decrease gradually with the frequency. When the thickness of water film is 0.085mm, the transmittance of wet radome is around -6dB and for each specific frequency, when the thickness of the water film increases from 0.085mm to 0.51mm with 0.085mm increment, the transmittance of the wet radome decreases about 2~3dB per step.

Then according to the theoretical settings, the experimental model is introduced based on extensive measurements of the reflectance and transmittance of the radome covered with various thicknesses of wet tissue paper. The same reflectance frequency response characteristics as the ones from the theoretical model are observed. Moreover, it is found that for each specific thickness of water film, the resonant frequency oscillates (less than 1GHz) with the range between the antenna and the radome in a similar trend, regardless of the thickness of the water film covered on the surface of the radome and this phenomenon can be caused by the near-field spherical wave effects. As to the transmittance of the wet radome from the experimental model, for each specific thickness of the water film, the transmittance of the wet radome decreases with the increasing frequency. For each specific frequency, when the thickness of the water film increases from 0.170mm to 0.510mm with 0.085mm increment, the transmittance of the wet radome decreases about 2~3dB per step which is the same as the result from the theoretical model.

Comparisons between these two models described in section 3.3 imply that generally the experimental results of wave propagation on the wet radome are consistent with the theoretical results, despite some small biases. Thus the theoretical model of wave propagation on the wet radome (75GHz~85GHz) is validated by the experimental model.

4

NUMERICAL MODEL FOR WAVE PROPAGATION ON WET RADOMES IN CST

In Chapter 3, though the theoretical model of wave propagation on the wet radome is generally validated with the experimental model based on real measurements, the biases between these two models may be assumed due to various factors such as temperature variance, measurement inaccuracy or near-field spherical wave effects. Moreover, the wet tissue mounted on the radome surface is a mixer of tissue, water and air, while for the theoretical model, the film on the radome surface is pure water only which makes it difficult to compare these two models and validate the conclusions. Thus in this chapter, a numerical model of wave propagation on the wet radome based on experimental settings is simulated in CST in order to further identify the applicability of the theoretical model. Besides, considering the fact that the wet radome may distort the antenna beam pattern which is important for the object angular estimation for modern radars, the water film effects on the antenna beam pattern are studied as well.

4.1. SETTINGS FOR THE SIMULATION IN CST BASED ON REAL MEASUREMENTS

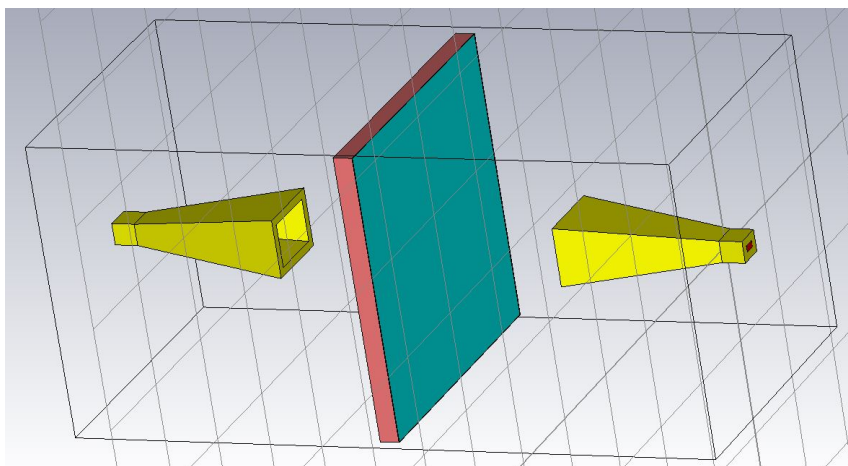


Figure 4.1: Settings for the simulation in CST based on real measurements

In order to better compare the numerical model with the experimental model of wave propagation on the wet radome, the settings of the simulation in CST are reconstructed as accurately as possible according to the previously experimental settings. Fig.4.1 shows the simulated model in CST (specific modeling steps are shown in appendix B) and the radome (pink) covered with the water film (blue) is vertically located in the middle of two antennas.

- Simulation of the horn antenna

The horn antenna used for the measurements is the standard gain horn series 27240-20 with dimensions of 32.5mm×12.4mm×9mm [11], working on 73.8GHz~112GHz and it is connected to the network analyser via a waveguide port with dimensions of 2.54mm×1.27mm. The material selected in CST for the horn construction is copper (annealed) which is used typically for the real antenna fabrication. Then the simulated antenna pattern at 77GHz and the antenna gain response with frequency are shown in Fig.4.2 and Fig.4.3 respectively.

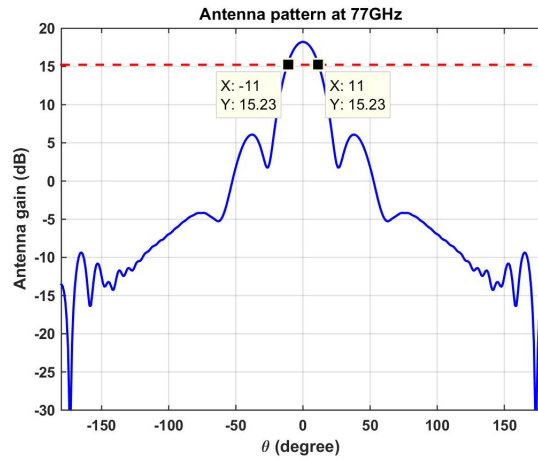


Figure 4.2: Simulated horn antenna pattern at 77GHz ($\phi = 0^\circ$)

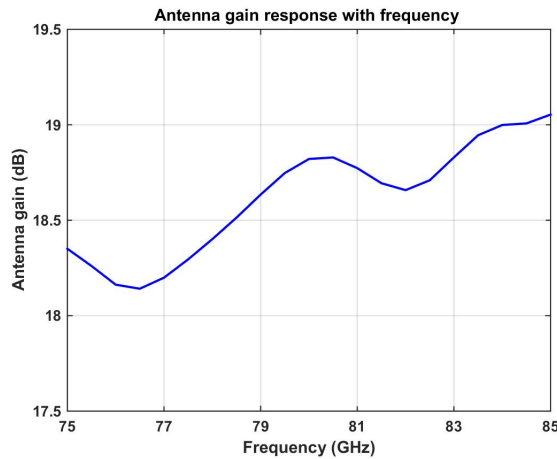


Figure 4.3: Simulated horn antenna gain response with frequency ($\phi = 0^\circ$, $\theta = 0^\circ$)

From Fig.4.2 and Fig.4.3, it can be seen that the 3-dB beam width of the simulated horn antenna at 77GHz is about 22° and the antenna gain generally increases with the frequency, about 18.35dB at 75GHz and 19.05dB at 85GHz. Both the simulated antenna 3-dB beam pattern at 77GHz and the antenna gain frequency response are consistent with real antenna characteristics described in the reference document [11].

- Dielectric constant of the radome and pure water in CST

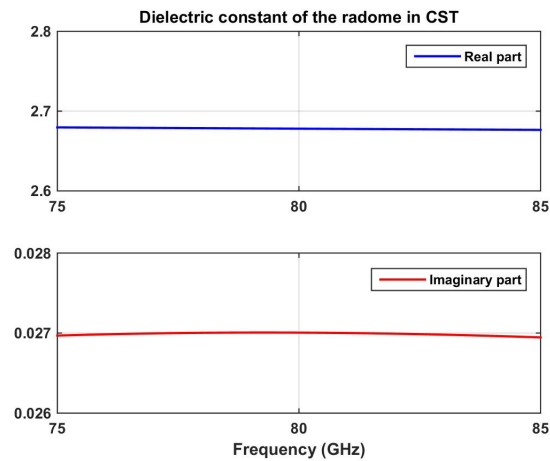


Figure 4.4: Simulated dielectric constant of the radome in CST

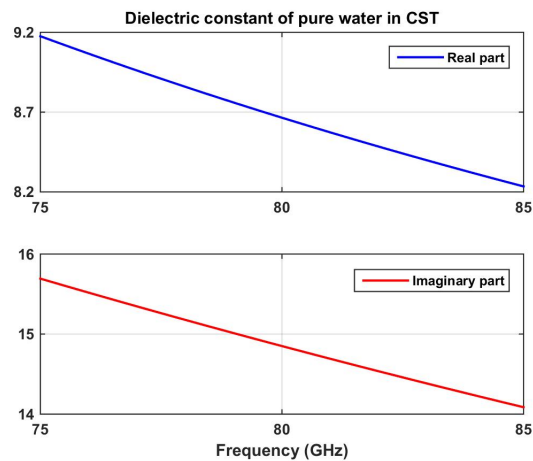


Figure 4.5: Simulated dielectric constant of pure water (17.5°C) in CST

Fig.4.4 shows the simulated dielectric constant of the radome over 75GHz~85GHz by selecting the 1st order fitting algorithm in CST. At the centre frequency of 80GHz, the simulated dielectric constant of the radome is exactly the same as the previously measured dielectric constant of the radome used for the derivation of theoretical and experimental models, namely 2.678-0.027j.

Fig.4.5 shows the simulated dielectric constant of the radome over 75GHz~85GHz by selecting the 1st order fitting algorithm in CST and the results are almost the same as the estimated dielectric constant of pure water (17.5°C) from D3M.

- Simulated size of the radome

The real size of the radome used for the experiments is 185mm×100mm×4.01mm. Considering the limited memory of computer to simulate such an electrically large radome at 75GHz~85GHz, the actual size of the radome set for the simulation is 30mm×30mm×4.01mm, still more than 20 times larger than the antenna beam footprint when the distance between antenna and the radome is 3cm (same distance as the real measurements). Thus the edge diffraction effect is effectively suppressed.

- Local mesh of the water film

Since the thickness of water film for the simulation is quite small (starts from 0.095mm) which may be less than the single edge of the meshed cells in CST, and then the simulated results can be inaccurate. Thus for the local mesh of the water film, the edge of the mesh cell responsible for the thickness of water film is set to be 1/8 thickness of the water film.

In all, the settings for the simulation are generally the same as the real experiments which helps better to compare the similarities and difference for the experimental, theoretical and numerical models.

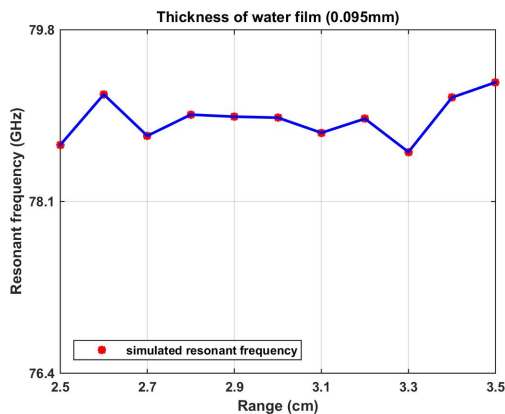
4.2. DERIVATION OF THE NUMERICAL MODEL FOR WAVE PROPAGATION ON THE WET RADOME

In CST, the simulated reflectance and transmittance of the radome covered with various thicknesses of the water film suffers from the free space propagation loss as well. In the same way, the reflectance from a perfect metal plate and the free space transmittance between two antennas are simulated for the calibration as we did in the real measurements.

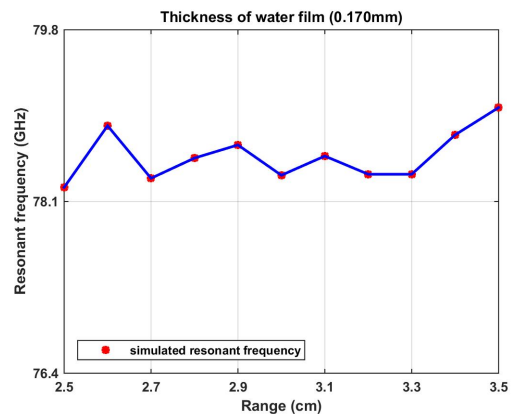
4.2.1. SIMULATED REFLECTANCE FROM THE BACKSIDE OF WET RADOME IN CST

- Position dependence of the resonant frequency of reflectance from the wet radome in CST

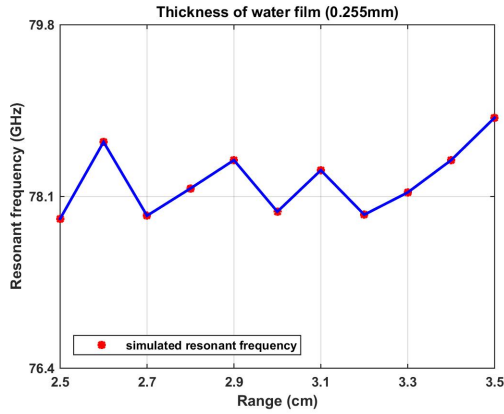
As we discussed in section 3.2.2, it is experimentally observed that the resonant frequency of reflectance from the wet radome depends on the position of the radome relative to the transmit antenna and this dependence is further studied in CST as well.



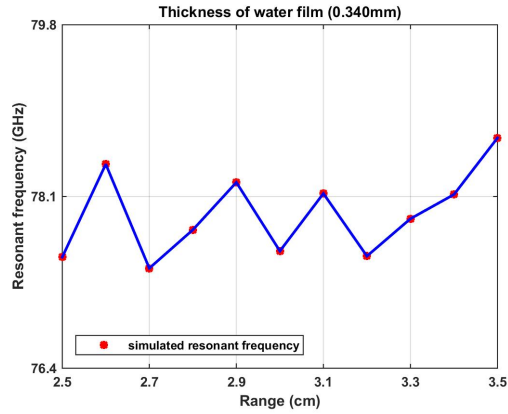
(a) 0.085mm



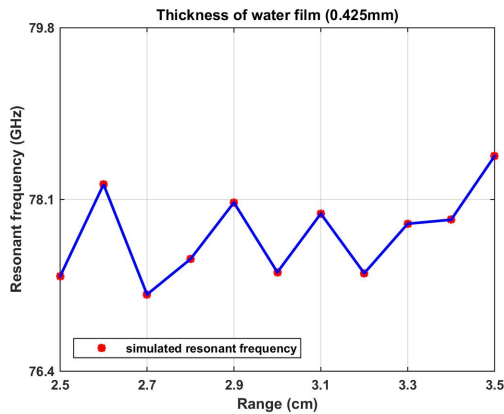
(b) 0.170mm



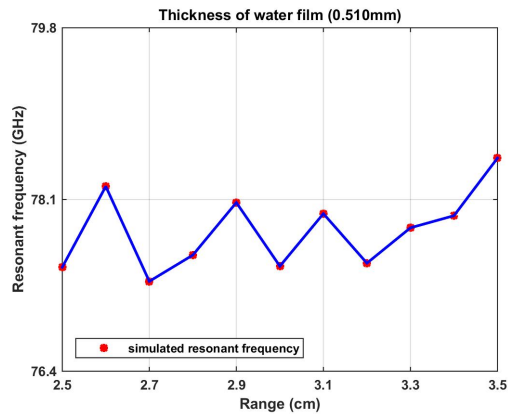
(c) 0.255mm



(d) 0.340mm



(e) 0.425mm



(f) 0.510mm

Figure 4.6: Variations of simulated resonant frequencies versus the range between the antenna and radome

Figure 4.6 shows the simulated resonant frequencies of the reflectance from the backside of wet radome when the range between the antenna and radome is increased from 2.5cm to 3.5cm. In each graph it can be observed that the resonant frequency of the reflectance from the wet radome oscillates with the relative range between the antenna and radome. Comparing the six graphs above, it can be seen that the resonant frequency oscillates with the range between the antenna and the radome in a similar trend, regardless of the thickness of the water film covered on the surface of the radome.

These observations from the simulation in CST are the same as the observations from the experimental results described in section 3.2 and these phenomena can be caused by the near-field spherical wave effects since the radome is quite close to the transmit antenna.

- Simulated mean reflectance from the wet radome in CST

Since the simulated resonant frequency of the reflectance from the backside of wet radome varies with the radome positions, and then the reflectance at each frequency element varies with the radome positions as well. In addition, the oscillation extent of the resonant frequency for each graph in Fig.4.6 is small, less than 1GHz. Thus the mean reflectance from the backside of wet radome among 11 simulations is calculated to suppress this effect.

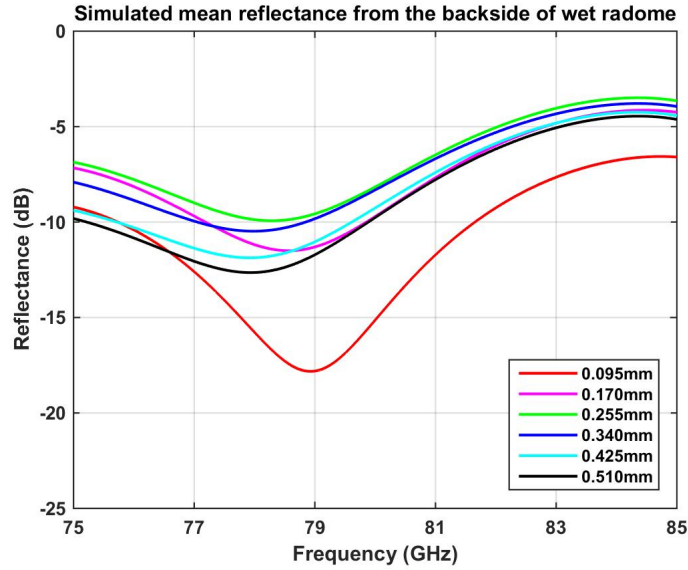


Figure 4.7: Simulated mean reflectance from the backside of radome covered with various thicknesses of the water film

Fig.4.7 shows the simulated mean reflectance from the radome covered by various thicknesses of water film from 75GHz to 85GHz among 11 simulations. In the same way as the experimental and theoretical results discussed previously, the reflectance from the backside of the wet radome for each specific thickness of water film primarily decreases with the frequency, reaching the minimum at the resonant frequency, and then starts to increase. When the thickness of water film increases from 0.095mm to 0.170mm, the variation of the reflectance frequency response curve is quite significant. While if the thickness of water film increases from 0.017mm until 0.510mm with 0.085mm per step, the variation of the reflectance frequency response curve is not as large as the thinner water film case. Furthermore, the reflectance frequency response curve becomes converged with the increase of the thickness of the water film. These phenomena are caused by the same reasons as we discussed in section 3.1.

The mean reflectance at the resonant frequency for each specific thickness is shown in Table 4.1 and it is observed that the resonant frequency shifts to a lower frequency with the increasing thickness of water film.

Table 4.1: Comparisons of simulated reflectance from the backside of radome covered with various thicknesses of water film

	0.095mm	0.170mm	0.255mm	0.340mm	0.425mm	0.510mm
MR (dB)	-17.82	-11.50	-9.93	-10.48	-11.87	-12.65
RF (GHz)	78.93	78.57	78.29	77.98	77.92	77.92

Note: **MR** : minimum reflectance; **RF**: resonant frequency;

4.2.2. SIMULATED TRANSMITTANCE OF THE WET RADOME IN CST

For the transmittance of the radome covered with each specific thickness of water film, a quite small amplitude bias can be observed among 11 simulations when the range between the antenna and radome is tuned from 2.5cm to 3.5cm. Thus the mean transmittance of the radome covered with each specific thickness of water film is calculated shown in Fig.4.8.

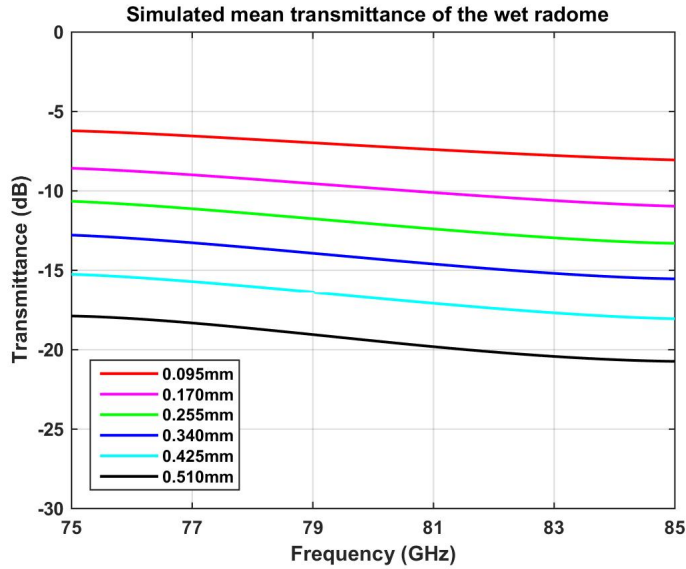


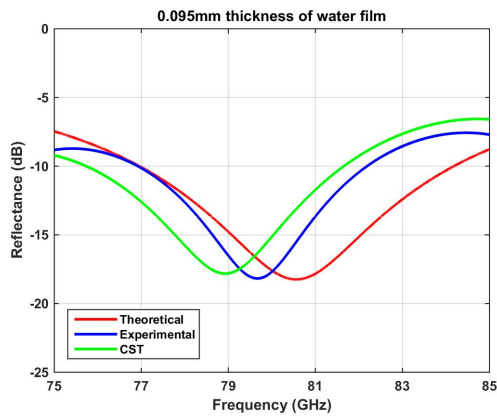
Figure 4.8: Simulated mean transmittance of the radome covered with various thicknesses of the water film

Fig.4.8 shows the simulated mean transmittance of the radome covered by various thicknesses of water film from 75GHz to 85GHz. For each specific thickness of the water film, the transmittance of the wet radome decreases with the increasing frequency. For each specific frequency, when the thickness of water film on the radome surface increases from 0.170mm to 0.510mm with 0.085mm per step, the transmittance of the wet radome decreases about 2~3dB per step. The mean transmittance of the radome covered with various thicknesses of water film at 75GHz and 85GHz are shown in Table 4.2.

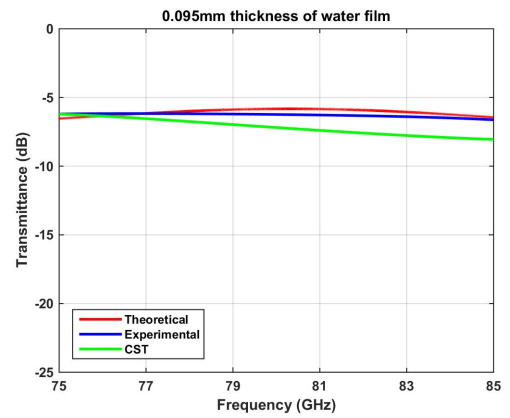
Table 4.2: Comparisons of simulated transmittance of the radome covered with various thicknesses of water film

	0.095mm	0.170mm	0.255mm	0.340mm	0.425mm	0.510mm
75 (GHz)	-6.22dB	-8.58dB	-10.67dB	-12.79dB	-15.26dB	-17.88dB
85 (GHz)	-8.05dB	-10.96dB	-13.30dB	-15.54dB	-18.04dB	-20.73dB

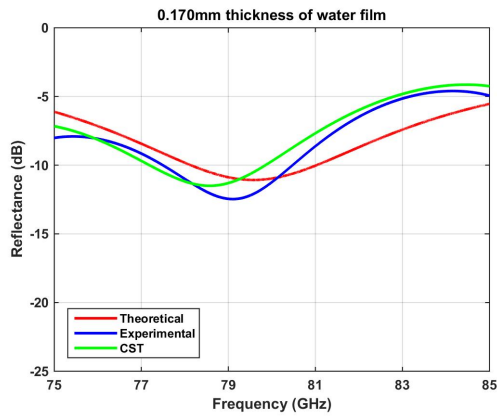
4.3. COMPARISONS OF THE NUMERICAL, EXPERIMENTAL AND THEORETICAL MODELS



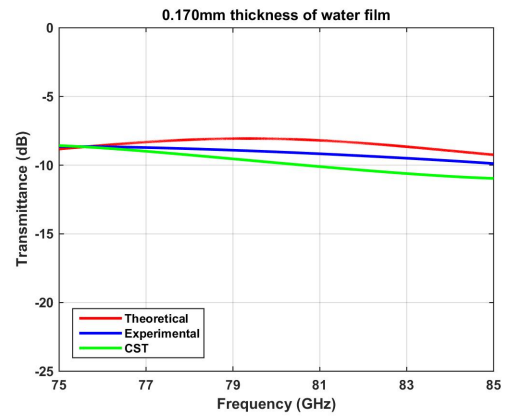
(a) 0.095mm



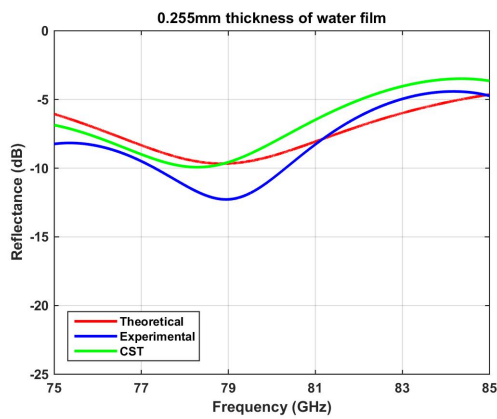
(b) 0.095mm



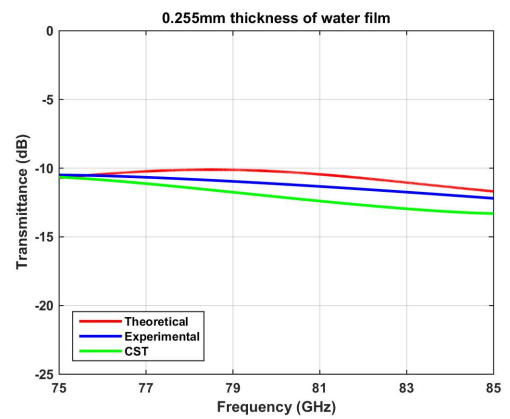
(c) 0.170mm



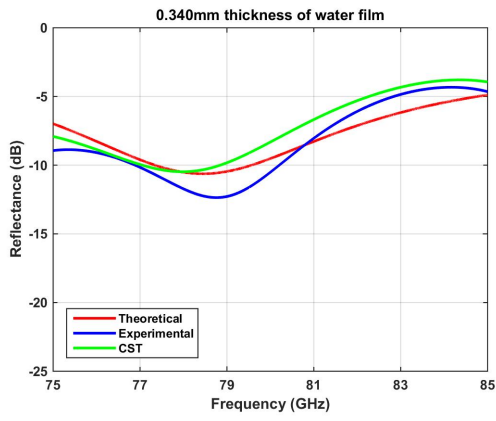
(d) 0.170mm



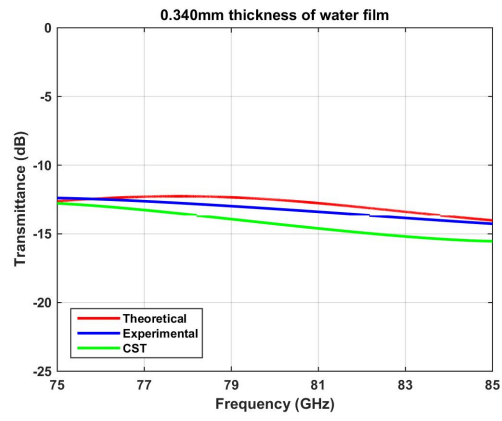
(e) 0.255mm



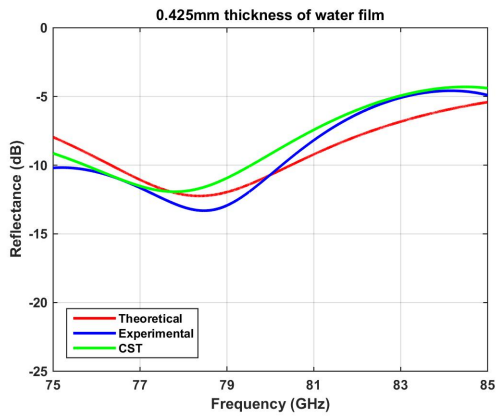
(f) 0.255mm



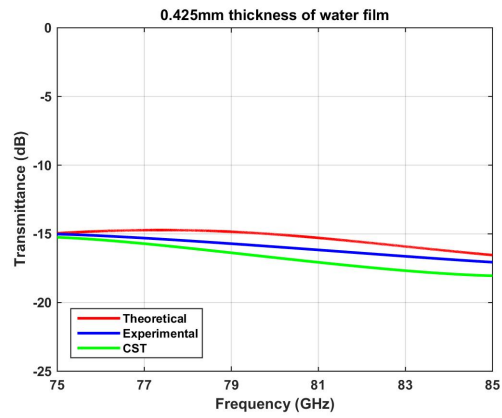
(g) 0.340mm



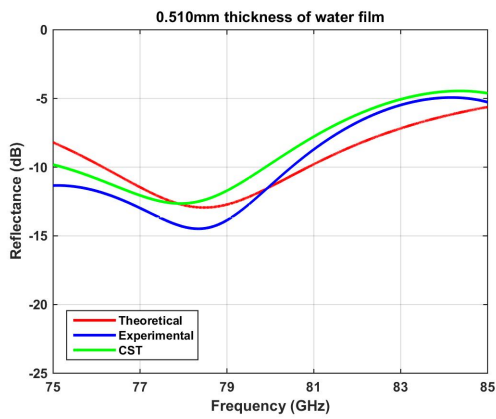
(h) 0.340mm



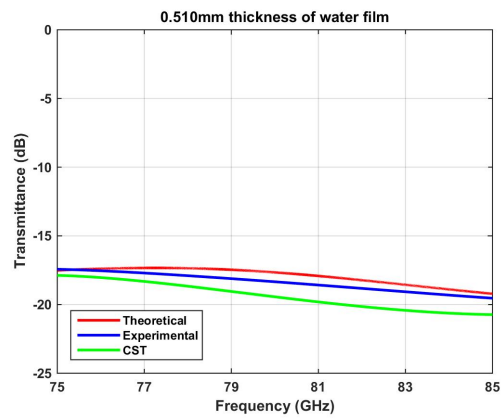
(i) 0.425mm



(j) 0.425mm



(k) 0.510mm



(l) 0.510mm

Figure 4.9: Comparisons of theoretical, experimental and numerical models for wave propagation on the wet radome

Fig.4.9 shows comparisons of numerical, theoretical and experimental models for wave propagation on the radome covered by various thicknesses of water film.

- Comparisons of resonant frequencies of the reflectance from three models

From each column in Table.4.3, it is observed that the resonant frequency decreases with the increasing thickness of water film in each model and when the thickness of water film is larger than 0.255mm, the resonant frequency becomes converged. Comparing each row in Table.4.3, it can be seen that the resonant frequency from the numerical model is always less than the one from theoretical model. When the thickness of water film is thin (less than 0.255mm), the resonant frequency bias between the theoretical and numerical model is noticeable, about 1~1.5GHz. When the thickness of water film is increased, this bias is decreased, about 0.5GHz.

Table 4.3: Comparisons of the resonant frequency of the reflectance from three models

	Theoretical model (GHz)	Experimental model (GHz)	Numerical model (GHz)
0.095mm	80.50	79.66	78.93
0.170mm	79.95	79.11	78.57
0.255mm	78.85	78.93	78.29
0.340mm	78.46	78.82	77.98
0.425mm	78.41	78.43	77.92
0.510mm	78.40	78.38	77.92

- Comparisons of the reflectance frequency response curves from three models

Comparing the reflectance curves from the numerical and theoretical model, it can be seen that the amplitude bias of these two models is mainly due to the frequency shift which means that the theoretical reflectance curve is roughly consistent with the numerical reflectance curve if the theoretical reflectance curve is shifted to the lower frequency band. While comparing the reflectance curves from the experimental and numerical models, the amplitude bias between these two models is mainly caused by the measurement inaccuracy.

- Comparisons of the transmittance of the wet radome from three models

From the right graphs in Fig.4.9, it is observed that the transmittance of the wet radome from the theoretical model is maximum in each graph and transmittance of the wet radome from the numerical model is minimum. The experimental transmittance of the wet radome slightly decreases with the increasing frequency, while the numerical transmittance of the wet radome significantly decreases with the increasing frequency. Generally, the bias of transmittance of the wet radome among three models is acceptable, less than 2dB.

Based on these observations, it is concluded that the near-field spherical wave effects on the wave propagation of the wet radome are insignificant, about 0.5~1.5GHz frequency shift for the reflectance and less than 2dB bias for the transmittance. Thus the theoretical model of wave propagation on the wet radome from 75GHz to 85GHz is both validated by the experimental and numerical models.

4.4. WATER FILM EFFECTS ON THE ANTENNA BEAM PATTERN (77GHz)

Nowadays multiple transmit and receive channels are built in the automotive radar and the target angle is estimated by comparing the amplitude ratios and phase differences of the received signals. The distortions of the antenna beam pattern caused by the wet radome might affect the accuracy of the angular estimation of the target. As a result, it is essential to study the water film effects on the antenna beam pattern and the simulated model (77GHz) in CST is shown in Fig.4.10.

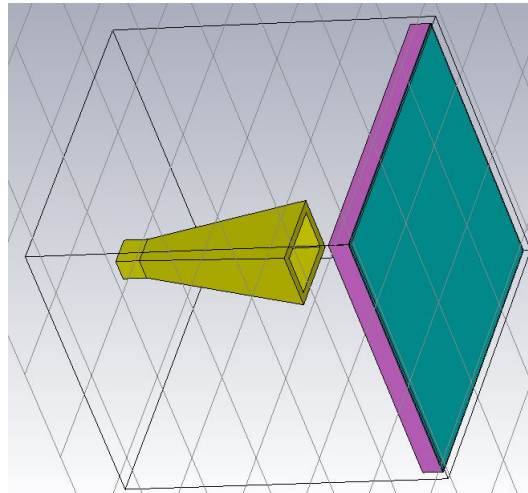
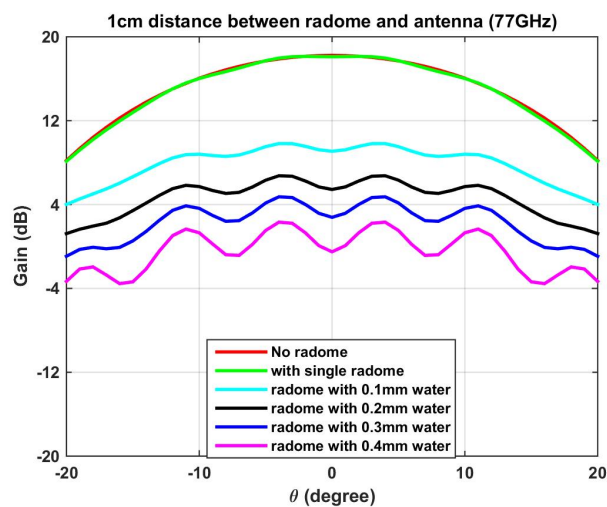
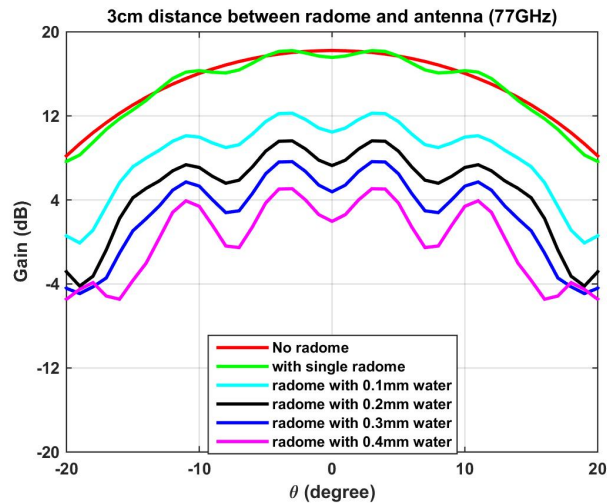


Figure 4.10: Simulated model of water film effects on the antenna beam pattern in CST

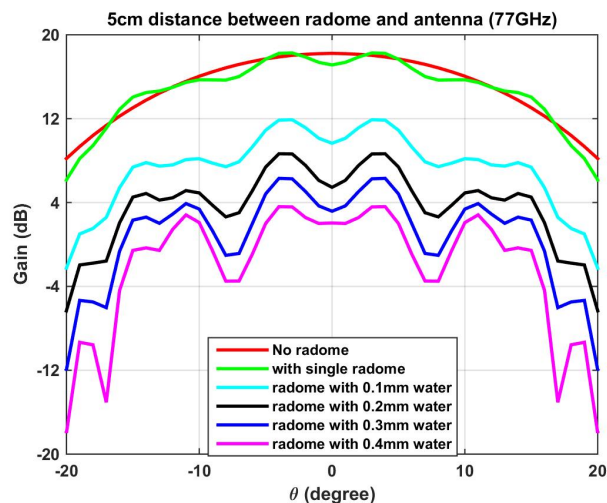
The dielectric constant of the well-designed radome in Fig.4.10 (size: 30mm×30mm×2.55mm, pink medium) is 2.33, same as the Polypropylene which is a common material for the bumper fabrication [12]. The radome is parallel to the horn antenna and distance between these two objects is set to be 1cm, 3cm and 5cm respectively which is the typical range between the transmitter and bumper for Continental radar[13]. Varying the thickness of water film (blue medium) from 0.1mm to 0.4mm with 0.1mm increase per step, the effects of the radome covered with various thicknesses of water film ($T=20^{\circ}\text{C}$) on the antenna beam pattern are shown in Fig.4.11 (a)~(c).



(a) 1cm distance between the antenna and wet radome



(b) 3cm distance between the antenna and wet radome



(c) 5cm distance between the antenna and wet radome

Figure 4.11: Water film effects on the antenna beam pattern

Fig.4.11 (a), (b) and (c) shows the effects of radome covered with various thicknesses of the water film on the antenna beam pattern when the distance between the transmit antenna and radome is 1cm, 3cm and 5cm respectively. For the single radome (no water) case, it is observed when the spacing between the radome and antenna is increased, the antenna beam distortion compared to the original beam pattern is more significant. Thus for an optimal performance, the radome should be as close as possible to the antenna and this conclusion is already confirmed in [3].

When the radome is covered with the water film, the antenna gain is dramatically decreased due to absorption. For a radome covered with a certain thickness of water film, when the spacing between the wet radome and antenna is increased, the antenna beam distortion is intensified which is the same as for a single radome case (no water). When the spacing between the wet radome and antenna is fixed, the beam distortion is intensified with the increasing thickness of the water film.

4.5. CONCLUSIONS

In this chapter, the numerical model of wave propagation on the wet radome (75GHz~85GHz) is simulated in CST based on the experimental settings. The comparisons between the theoretical, numerical and experimental models are discussed.

For the reflectance from the backside of wet radome, the resonant frequency from the theoretical model is maximum, while the resonant frequency from the numerical model is minimal. The numerical and experimental reflectance frequency response curves can be roughly obtained by shifting the theoretical reflectance frequency response curve to a lower frequency band. For the transmittance of the wet radome, it decreases significantly with the increasing frequency from the numerical model. While in the experimental model, it decreases roughly with the frequency. Generally, the bias of transmittance of the wet radome in three models is acceptable, less than 2dB. These phenomena can be caused by the near-field spherical wave effects. Based on the observations above, it is concluded the near-field spherical wave effects on the wave propagation of the wet radome are insignificant, about 0.5~1.5GHz frequency shift for the reflectance and less than 2dB bias for the transmittance. Thus the theoretical model of wave propagation on the wet radome from 75GHz to 85GHz is both validated by the experimental and numerical models.

In addition, the water film effects on the antenna beam pattern are studied. From the simulation results in CST, we find that for a single radome case, the radome should be as close as possible to the antenna in order to keep better radar performance which is already confirmed in [3]. When the radome is covered with the water film, the antenna gain is dramatically decreased due to absorption. For a radome covered with a certain thickness of water film, when the spacing between the wet radome and antenna is increased, the antenna beam distortion is intensified which is the same as the result for a single radome case (no water). When the spacing between the wet radome and antenna is fixed, the beam distortion is intensified with the increasing thickness of the water film.

5

ESTIMATION OF STATISTICAL ROUGHNESS OF THE LAYER SURFACE

When the radar signal passes the radome/bumper, reaching the road or other components of road/highway infrastructure, the backscattered signal from these objects can be a quite useful source of information for cars local real-time navigation on the road. To make such observation reliable, the road signs are required to have reasonably big radar cross section in a wide range of observation angles which is mainly determined by the surface roughness. At automotive frequency band, the wavelength is only about 4mm. Thus the back-scattered signals strongly depend on the characteristics of the thin layer of the paint on the surface of the road or road infrastructure. Based on these facts, three radar detectable paint samples with rough surfaces are experimentally studied. Then by tuning the parameters of the derived model of backscatter coefficient of the single medium with rough surface to fit the measured results, the statistical roughness of the surfaces of these three paint samples can be estimated. Such information about the roughness of the radar detectable paint samples can be quite useful for the future road or road infrastructure paint design, aiming to improve objects' detectability with the automotive radar.

5.1. THEORETICAL CALCULATION OF THE BACKSCATTER COEFFICIENT FOR A ROUGH SURFACE

The scattered signals from a rough surface consist of two components, namely the coherent scattering and incoherent scattering [14]. The coherent scattering reacts as a specular reflection on a smooth surface which cannot be received by the monostatic radar. While the incoherent component is the diffuse backscattering, distributing the scattered power in all directions. When the medium surface becomes rougher, the coherent scattering is weaker and the incoherent backscattering turns to dominate.

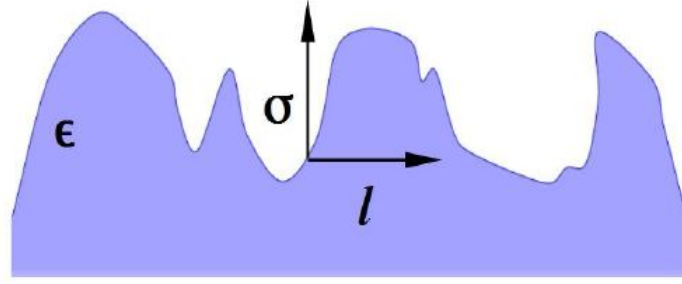


Figure 5.1: Geometry of the rough surface of a single layer

Fig.5.1 shows the rough surface of a single layer with the dielectric constant ϵ locating in the free space. σ [m] is the root-mean-square height of the roughness which characterizes the dispersion of the surface height relative to the reference plane. ℓ [m] is the characteristic horizontal scale of the roughness which describes the horizontal width of the bump.

The roughness of the surface is assumed to be small, mildly sloping and statistically isotropic. The backscatter coefficients of the rough surface of a single layer for vertical and horizontal polarizations are given by [15]:

$$\sigma_{\nu 0}(\theta, \phi) = 4k_0^4 |\epsilon - 1|^2 \cos^4 \theta \hat{B}(-2\vec{k}) \cdot |\epsilon \sin^2 \theta + (\epsilon - \sin^2 \theta)|^2 / |\epsilon \cos \theta + (\epsilon - \sin^2 \theta)^{\frac{1}{2}}|^4 \quad (5.1)$$

$$\sigma_{h0}(\theta, \phi) = 4k_0^4 |\epsilon - 1|^2 \cos^4 \theta \hat{B}(-2\vec{k}) / |\cos \theta + (\epsilon - \sin^2 \theta)^{\frac{1}{2}}|^4 \quad (5.2)$$

where:

k_0 : Wavenumber in free space;

ϵ : Dielectric constant of the medium;

θ, ϕ : Incident angle and azimuth angle respectively;

\vec{k} : A vector given by $\vec{k} = k_0 \sin \theta (\vec{x}_0 \cos \phi - \vec{y}_0 \sin \phi)$

\hat{B} : The spatial spectrum of the interfaces corrugations, given by $\hat{B}(-2\vec{k}) = \sigma^2 \ell^2 e^{-2k_0^2 \ell^2 \cos^2 \theta}$ for the statistically isotropic roughness of the surface [16].

Here σ and ℓ is the root-mean-square height and the characteristic horizontal scale of surface roughness mentioned previously. Thus if the backscatter coefficient versus incident angles for a rough surface of unknown material can be measured, it is possible to estimate the value of σ and ℓ for this surface roughness by applying equation (5.1) and (5.2). In order to achieve this, it is essential to know how the backscattering coefficient depends on these parameters.

Fig.5.2~Fig.5.4 shows the results of the dielectric constant (ϵ) dependency, root-mean-square height (σ) dependency and horizontal roughness (ℓ) dependency of the backscattering coefficient from the rough surface respectively.

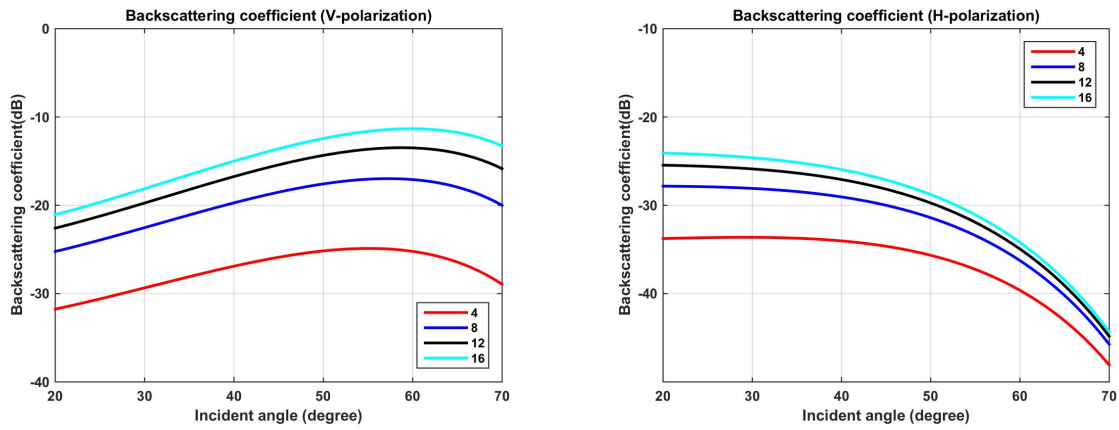


Figure 5.2: Dielectric constant (ϵ) dependency of the backscattering from the rough surface for H,V polarization ($\sigma=0.3\text{mm}$, $\ell=0.5\text{mm}$)

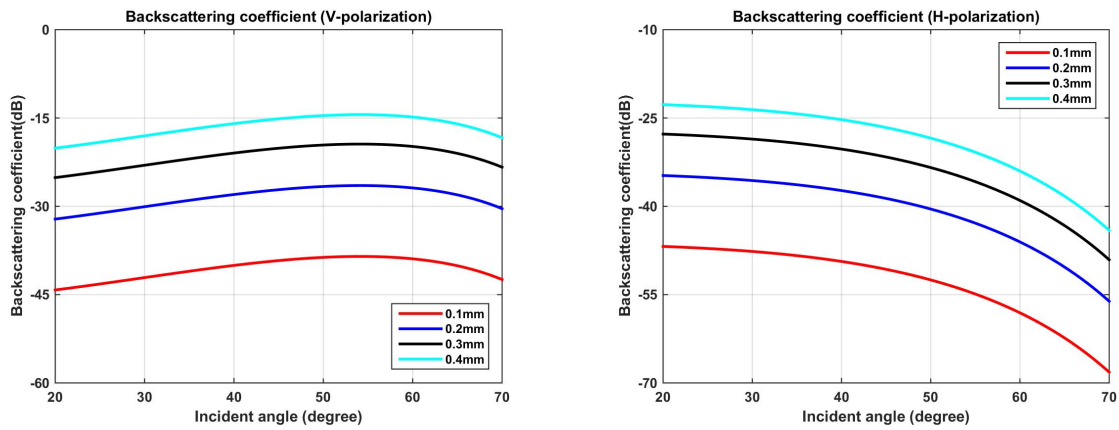


Figure 5.3: Root-mean-square height (σ) dependency of the backscattering from the rough surface for H,V polarization ($\epsilon=8$, $\ell=0.4\text{mm}$)

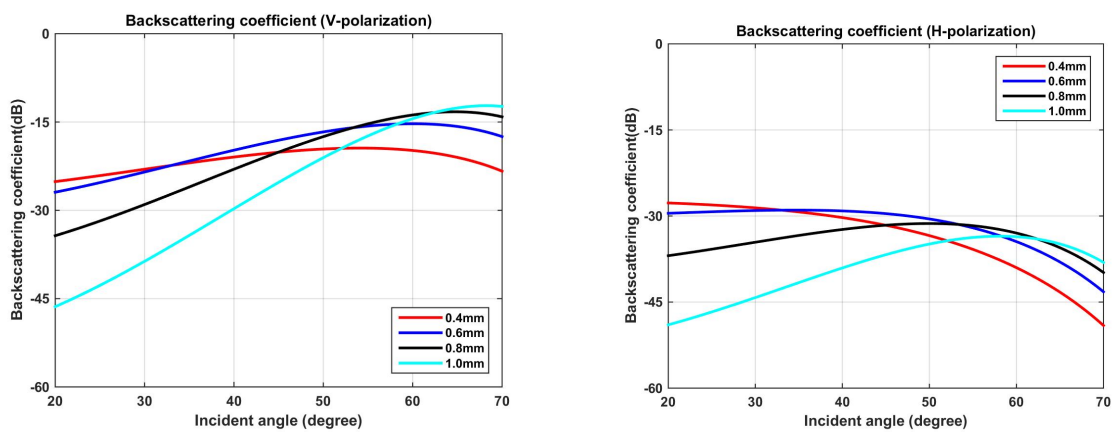


Figure 5.4: Horizontal roughness (ℓ) dependency of the backscattering from the rough surface for H,V polarization ($\epsilon=8$, $\sigma=0.3\text{mm}$)

From Fig.5.2~Fig.5.4, it can be observed that

- The dielectric constant (ϵ) of the medium mainly changes the intensity of the backscattering on the rough surface for both vertical and horizontal polarizations. The larger of the dielectric constant, the stronger backscattering we can expect.
- The root-mean-squared height of roughness (σ) mainly changes the intensity of the backscattering on the rough surface for both vertical and horizontal polarizations. The rougher of the surface in vertical direction (larger σ), the stronger of the backscattering we can expect
- The horizontal scale of the surface roughness (ℓ) mainly changes the slope as well as the trend of backscattering angular response curve for both vertical and horizontal polarizations.

In all, the intensity of the backscattering on the single rough surface is mainly determined by the medium dielectric constant and the root-mean-square height of the surface roughness. While the slope and the trend of the backscattering angular response curve is mainly determined by the horizontal scale of the roughness. These observed results provide the important guidance to estimate the statistical roughness of the unknown rough surface which will be discussed later.

5.2. MEASUREMENTS OF THE BACKSCATTERING COEFFICIENT OF THE ROUGH SURFACE

5.2.1. EXPERIMENTAL SETTINGS

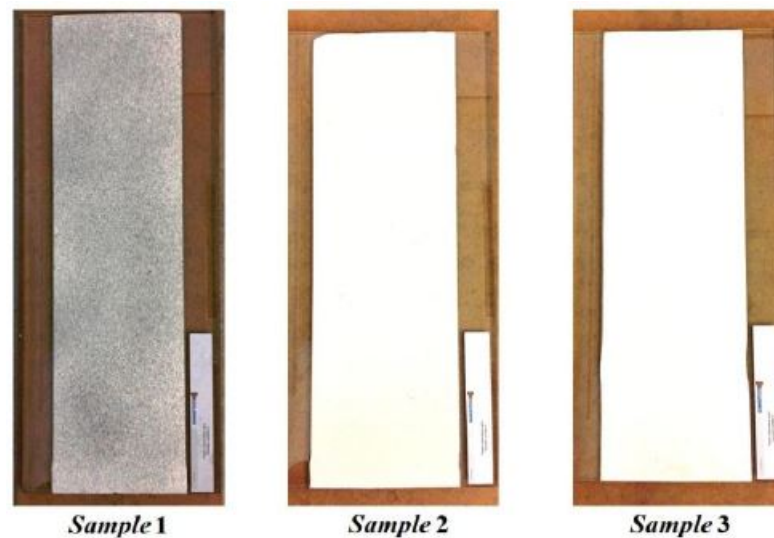


Figure 5.5: Three radar detectable paint samples for the measurements

Fig.5.5 shows three quite thin radar detectable paint samples coated on the glass. Each paint sample with dimensions of 60cm×20cm specifically owns discrete inclusions inside which provides a rough surface for the experiments.



Figure 5.6: Experimental setting for the measurements of backscattering from rough surfaces

The mono-static backscattering of the paint sample is measured by the network analyser at three different frequency bands, namely 75GHz~85GHz, 85GHz~95GHz and 95GHz~105GHz. The paint sample is mounted vertically on a rotating stick shown in Fig.5.6 and with such a rotator, the incidence angle can be tuned from 0° to 90° with 5° increments.

5.2.2. BACKSCATTERING COEFFICIENTS OF THE ROUGH SURFACE BASED ON REAL MEASUREMENTS

The experimental road sample is an extensive target with a size of $60\text{cm} \times 20\text{cm}$ and its radar cross section depends on the illuminated area. Thus it is characterised with the backscattering coefficient, given as [17]:

$$\sigma_0 = \frac{\langle \sigma \rangle}{A} \quad [\textit{unitless}] \quad (5.3)$$

where $\langle \sigma \rangle$ is the statistical average radar cross section [m^2], A is the illuminated area [m^2]. From the basic radar range equation, the radar cross section can be calculated as [18]

$$\sigma = \frac{P_r (4\pi)^3 R^4}{P_t G^2 \lambda^2} \quad [m^2] \quad (5.4)$$

where R is the range of the target, P_t is the transmitted power, P_r is the received power, G is the antenna gain and λ is the free space wavelength. The back scattered power measured by the network analyser is calibrated by measuring the power from a metal plate. For a metal plate with normal incidence, the received power is the transmitted power attenuated with the free space loss. Then the ratio of the received power and transmitted power is

$$\frac{P_r}{P_t} = G^2 \left(\frac{\lambda}{4\pi R} \right)^2 \quad (5.5)$$

Substituting equation (5.5) to (5.4), the effective radar cross section of the metal plate can be given as

$$\sigma = 4\pi R^2 \quad (5.6)$$

The area of the antenna footprint on the sample can be given as

$$A = 4R^2 \tan \frac{\theta_E}{2} \tan \frac{\theta_H}{2} \csc \theta \quad (5.7)$$

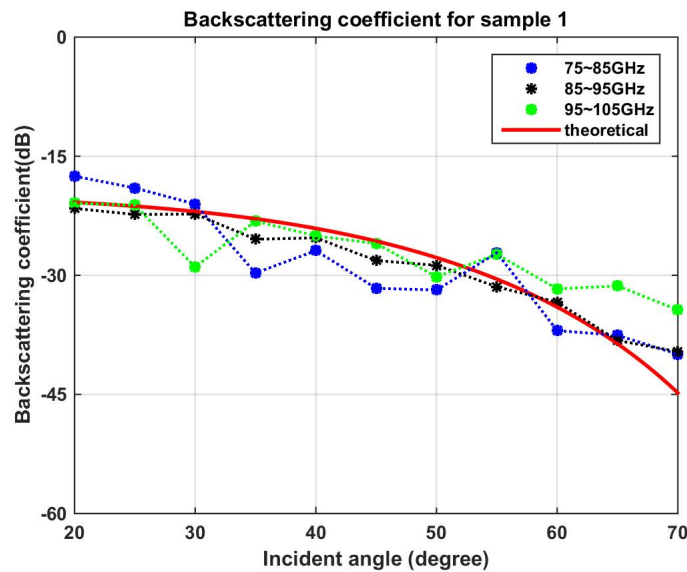
Here θ_E , θ_H is the antenna 3-dB beam width in the E and H plane respectively and θ is the incident angle. Thus the calibrated backscattering coefficient of the rough surface can be given as

$$\sigma_{norm} = \frac{\hat{P}_{sample}}{P_{metal}} \frac{\pi}{\tan(\theta_E/2) \tan(\theta_H/2) \csc \theta} \quad (5.8)$$

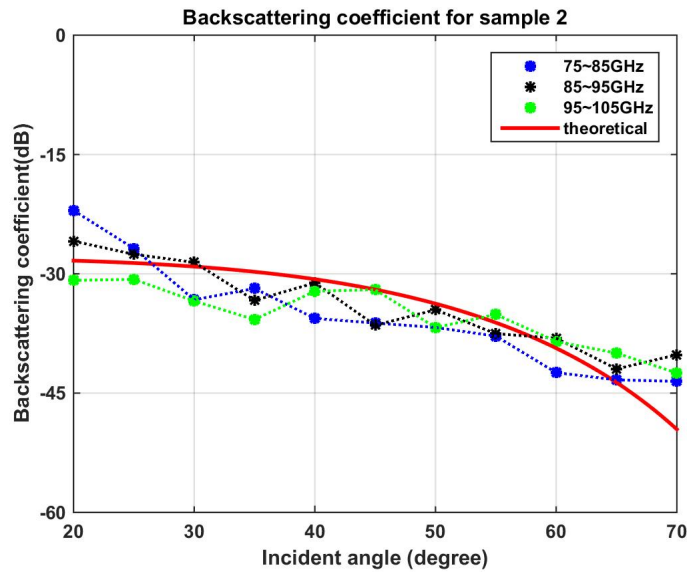
where \hat{P}_{sample} is the measured mean backscattered power from the sample surface and P_{metal} is the measured backscattered power from the metal with normal incidence.

5.2.3. MEASURED BACKSCATTERING COEFFICIENTS FOR THREE PAINT SAMPLES

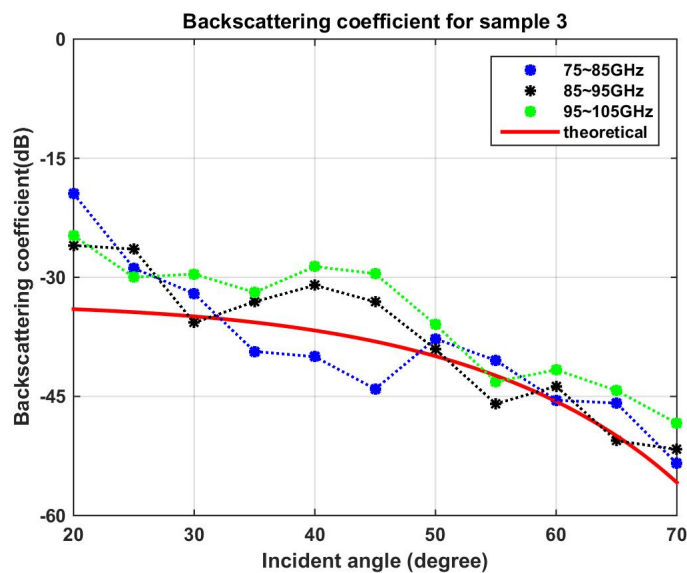
Since we are only interested in the incoherent scattering of the rough surface, the incident angle is set to be $20^\circ \sim 70^\circ$ for the experiments. The measured backscattering coefficients versus incident angles for three paint samples at different frequency bands as well as correspondingly theoretical fitting lines are shown in Fig.5.7(a)~(c) respectively.



(a) Sample 1



(b) Sample 2



(c) Sample 3

Figure 5.7: Measured backscattering coefficients versus incident angles for sample 1, 2 and 3

Fig.5.7 (a), (b) and (c) describes the measured backscattering coefficient versus incident angles at different frequency bands for paint sample 1, paint sample 2 and paint sample 3 respectively. It can be observed that the backscattering from all three sample surfaces decreases with the incident angle and in general, the backscattering on the surface of sample 1 is maximum, while backscattering from sample 3 is minimum. When the incident angle is increased from 20° to 70° , the backscattering coefficient for both sample 1 and sample 2 decreases about 20dB, while for sample 3, it decreases about 30dB. In addition, the frequency dependency of backscattering for sample 1 and sample 2 is not significant. While for sample 3 in Fig.5.7 (c), it can be seen that when the incident angle is between 35° ~ 50° , the frequency dependence of the backscattering coefficient is noticeable and this can be caused by the interference.

Since the antenna polarization for the measurements is horizontal (E field perpendicular to the plane of incidence), and then by applying equation (5.2), the theoretical fitting curve (red) of the backscattering angular response is obtained for each sample and the estimated dielectric constant (ϵ) and statistical roughness (σ, ℓ) for each sample are shown in Table.5.1

Table 5.1: Estimated dielectric constants and the statistical roughness for experimental samples

	Dielectric constant ϵ	RMS height roughness σ	Horizontal roughness ℓ
Sample 1	18	0.35mm	0.40mm
Sample 2	12	0.25mm	0.45mm
Sample 3	9	0.20mm	0.40mm

As we discussed in section 5.1, the intensity of the backscattering coefficient for the rough surface is determined both by the dielectric constant and the RMS height roughness, thus multiple combinations of estimations for these two parameters of the sample surface exist.

5.3. CONCLUSIONS

In this chapter, the theoretical calculation of backscattering coefficient for the rough surface of a single layer is introduced and discussed. It is found that the intensity of backscattering coefficient is mainly determined by the dielectric constant of the medium and the root-mean-squared height of the surface roughness for both vertical and horizontal polarizations. While the horizontal scale of the surface roughness determines the trend and slope of the backscattering angular response curve.

Then the measurements of backscattering from the surfaces of three radar detectable paint samples at three different frequency bands are performed. By tuning the theoretical parameters in equation (5.2), we are able to estimate the statistical roughness of the measured sample surface when the curve of theoretical backscattering angular response fits the measured one. These estimated information about radar detectable paint samples can be quite useful for the future road or road infrastructure design, aiming to improve objects' detectability with the automotive radar.

6

CONCLUSIONS AND FUTURE WORK

6.1. CONCLUSIONS

The major goal of this project is to investigate the water film effects on the wave propagation on the radome over the whole automotive frequency band (75GHz~85GHz).

In order to study these effects, three wave propagation models ($T=17.5^{\circ}\text{C}$) are derived, namely the theoretical model based on plane wave assumptions, the experimental model based on extensive real measurements and the numerical model simulated in CST. For the experimental model and numerical model, since the distance between the antenna and wet radome does not fulfill the far field criterion $R \geq 2D^2/\lambda$, and then the near-field spherical wave effects are included. Comparing these three models, it is concluded that

- The existence of water film on the radome ($\epsilon = 2.678 - 0.027j$, thickness: 4.01mm) surface can significantly change the characteristics of reflectance from the backside of wet radome. For each specific thickness of water film covered on the radome surface, there is a corresponding resonant frequency where the minimum reflectance occurs over the whole bandwidth and this resonant frequency decreases with the increasing thickness of water film. When the water film is thin, the reflectance frequency response curve is quite sensitive to the thickness of water film. When the thickness of water film is larger than 0.255mm, the reflectance frequency response curve is becoming converged with the increasing thickness of water film. These observations imply that the thickness optimization of multiple half wavelengths for a single dry radome [19] is not applicable for wet radome because in reality the thickness of the water film covered on the radome surface is random (falling rain drops, splashes from the road, etc.) and the reflectance from the backside of the wet radome is quite sensitive to the thickness of thin water film. Then other radome optimization design needs to be explored.
- When the thickness of water film covered on the radome surface is 0.17mm, the transmittance of the wet radome is about -9dB. For each specific frequency, the transmittance of the wet radome decreases about 2~3dB per step when the thickness of the water film increases from 0.17mm to 0.51mm with 0.085mm per step. These results demonstrate that the one-way attenuation caused by the extra water film can severely limit the radar efficiency and maximum radar detection range.
- Generally the experimental and numerical results are consistent with the theoretical results. From the experimental and numerical model, we find the resonant frequency of the reflectance from the backside of the wet radome oscillates with the range between the radome and antenna and the resonant frequency from these two models is a bit smaller than the one from theoretical model. This resonant frequency bias (0.5GHz~1.5GHz) can be caused by the near-field spherical wave effects. As to the transmittance of the wet radome from three models, it is observed the transmittance of the wet radome from the theoretical model is

always maximum and transmittance of the wet radome from the numerical model is minimum. Generally, the bias of transmittance of the wet radome among three models is acceptable, less than 2dB.

Though the numerical model in CST considers all conditions, the processing is quite time-consuming, about 2 hours. While the processing for the theoretical model in MATLAB can finish instantly. Thus the theoretical model of wave propagation on the wet radome is more applicable in reality.

Moreover, the water film effects on the antenna beam pattern are investigated. It is found that when the radome is covered with the water film, the antenna gain is dramatically decreased due to absorption and the existence of the water film will further intensify the antenna beam distortion caused by the single radome. In addition, for a radome covered with a certain thickness of water film, when the spacing between the wet radome and antenna is increased, the antenna beam distortion is increased which is the same as for a single radome case (no water).

Finally, the statistical roughness of the surfaces of three radar detectable paint samples are estimated from equation (5.1) and (5.2). These two equations suggest that the intensity of the backscattering on the rough surface is mainly determined by the medium dielectric constant and the root-mean-squared height of roughness. While the slope and the trend of backscattering angular response curve is mainly determined by the horizontal scale of the roughness. Such surface roughness information can be quite useful for the future road or road infrastructure design, aiming to improve objects' detectability with the automotive radar.

6.2. FUTURE WORK

- The derived wet-radome models are easily to be transferred to be the dirt-radome or snow-radome models by replacing the water film layer. Thus the dirt and snow film effects on the wave propagation on the radome can continually be investigated in order to further improve the reliability of automotive radar.
- The numerical model in CST takes around two hours for each simulation at mm-wave frequency, thus we can try to find a more applicable and efficient way to obtain the numerical model, by optimizing the simulation method in CST or selecting another software to simulate.
- Though in our project, it is already demonstrated that the near-field spherical wave effects do not significantly influence the wave propagation on the wet radome. It is still meaningful to further study the near-field effects considering the fact that the radome is located quite close to the sensor in the car.

A

DETERMINATION OF THE DIELECTRIC PROPERTIES OF THE RADOME

The dielectric constant of the radome used for our project is unknown, thus primarily the dielectric constant of the radome is determined by the measurements.

A.1. THEORETICAL ANALYSIS OF THE FREE SPACE TECHNIQUE

For the free-space transmission technique, the material sample ($\epsilon = \epsilon' - j\epsilon''$) is placed between a transmitting antenna and a receiving antenna, and the attenuation and phase shift are measured to determine the sample dielectric permittivity. The dielectric constant (ϵ') is derived from the phase shift ($\Delta\phi$, degree) between the phase angle (ϕ , degree) measured with the sample and the phase angle (ϕ_0 , degree) measured without the sample, namely

$$\Delta\phi = \phi - \phi_0 = -360 \frac{d}{\lambda_0} \sqrt{\epsilon} + 360 \frac{d}{\lambda_0} = -360 \frac{d}{\lambda_0} (\sqrt{\epsilon} - 1) \quad (\text{A.1})$$

where d is the sample thickness [m] and λ_0 is the free space wavelength [m]. Considering the fact of phase ambiguity in the real measurements, equation (A.1) can be expressed as

$$\Delta\phi = \varphi - 360n \quad (\text{A.2})$$

where φ is the reading of the instrument ($-180^\circ \leq \varphi \leq 180^\circ$) and n is an integer ($n \geq 0$).

When the plane wave is normally travelling through a low-loss layer ($\epsilon'' \ll \epsilon'$), the real part of the dielectric constant can be approximately determined as [20]:

$$\epsilon' \approx \left(1 + \frac{\Delta\phi\lambda_0}{360d}\right)^2 \quad (\text{A.3})$$

As to the dielectric loss factor ϵ'' , it is estimated based on the measured transmittance of the sample. For a low-loss layer, equation (2.23) is applied to calculate the theoretical transmittance of the single sample film. By tuning the value of dielectric loss factor ϵ'' between 0~0.1, it is possible to find the reasonable estimation of ϵ'' when the calculated theoretical transmittance of the sample film is best fitting the measured transmittance of the sample film.

A.2. REAL MEASUREMENTS OF THE DIELECTRIC PROPERTIES OF THE RADOME

The Vector Network Analyser (N5260-60003,VNA) operating from 67GHz to 110GHz is used to perform all the measurements. Two w-band (73.8-112GHz) pyramid horn antennas with approximate 22° 3-dB beam width are used as a transmitter and a receiver. Normally the instrument measures the S-parameters and displays the results in the frequency domain.

- Experimental settings

Fig.A.1 shows experimental settings for the measurements of dielectric properties of the radome. The operational frequency range of the network analyser is set to be 75GHz~85GHz and distance between two antennas is 6cm. The radome with a size of 18.5cm \times 10cm which is large enough to suppress the diffraction effects at the edge, is vertically located in the middle of two antennas so that most of the power will be normally transmitted. As to the thickness of the radome, it is about 4.01mm measured by the calliper with 0.005mm accuracy.



Figure A.1: Experimental settings for the measurements of the dielectric properties of the radome

- Measurement results of the real part of the dielectric constant of the radome

In section A.1, we already known for a low-loss material, the real part of the dielectric constant of the sample can be estimated from the phase difference between the phase measured with the sample and the phase measured without the sample. For a single experiment, the measured original phase angles and the phase difference between these two cases are shown in Fig.A.2.

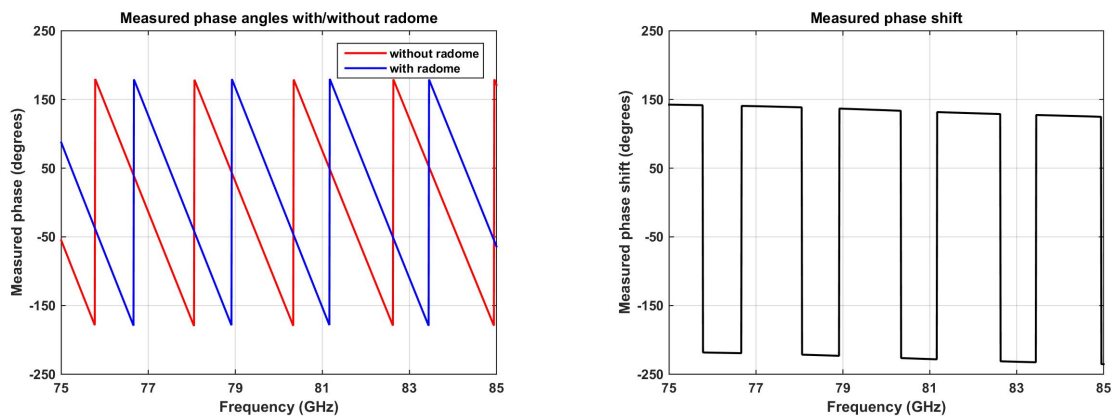


Figure A.2: Measured phase angles with/without the radome and the corresponding phase shift

From the published data and the preliminary measurements, the real part of dielectric constant of the radome should be around 2-3 and since the thickness of this sample radome is 4.01mm, the expected phase shift calculated from equation (A.1) should be around $-299.42^\circ \sim -149.49^\circ$. In the left graph of Fig.A.2, it is observed that when the phase reading of the instrument reaches -180° , it transfers instantly to 180° . Thus the measured positive phase shift (shown in the right graph of Fig.A.2) needs to subtract 360° to remove the phase ambiguity. Finally the actual phase shift after removing the phase ambiguity and the corresponding real part of the dielectric constant ϵ' calculated from equation (A.3) are shown in Fig.A.3.

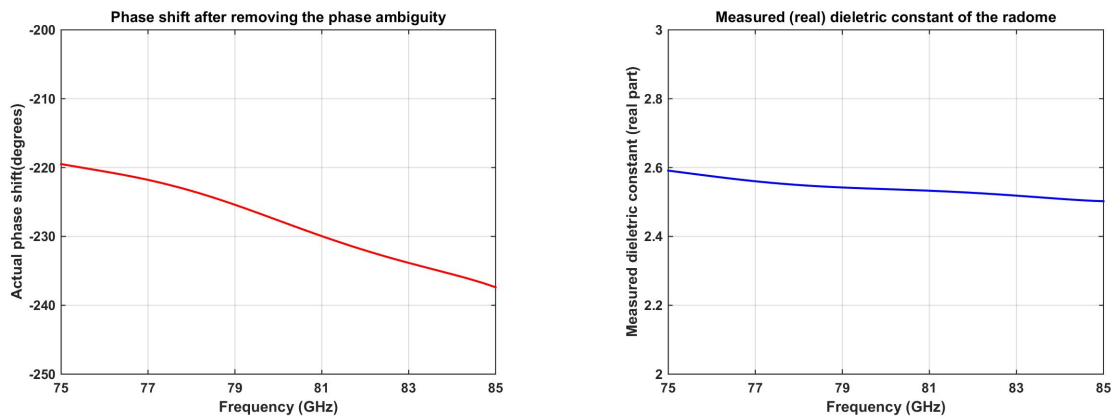


Figure A.3: Actual phase shift and the corresponding real part of the dielectric constant of the radome

- Measurement results of the reflectance and transmittance of the single radome

In the meanwhile, the measurements of the reflectance and transmittance of the radome with normal incidence are performed. Due to the imperfect orientation alignment of the radome, two antennas as well as the metal plate used for the calibration, each measurement is repeated independently 20 times. The averaged reflectance and transmittance of the radome as well as the corresponding root mean squared error (RMSE) are shown in Fig.A.4.

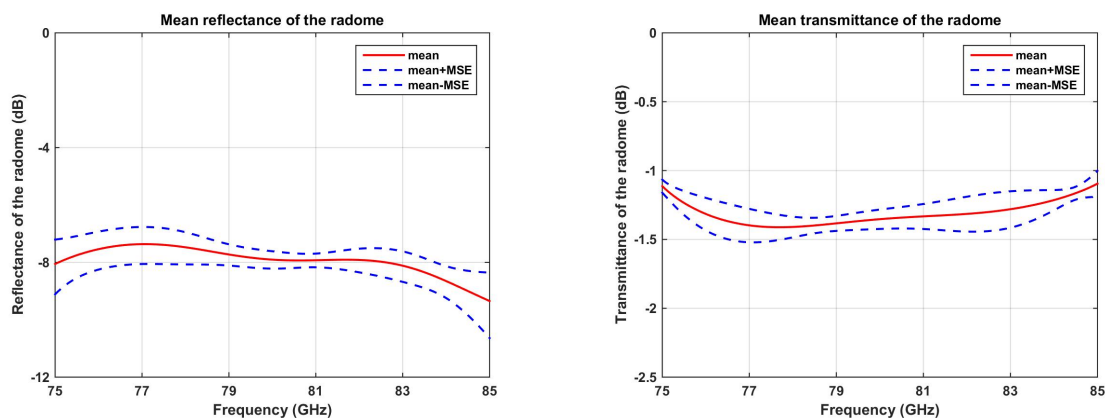


Figure A.4: Measured mean reflectance/transmittance of the single radome and the corresponding mean squared errors

From Fig.A.4, it is observed that the reflectance and transmittance of the radome is around -8dB and -1.25dB respectively. The variance of the reflectance of the radome among 20 measurements is generally less than 1dB, larger than the variance of the transmittance among 20 measurements and it is because the measured reflectance of the sample is quite sensitive to the orientation alignment of the radome and the metal plate used for calibration.

A.3. DETERMINATION OF THE DIELECTRIC CONSTANT OF THE RADOME

In section A.2, the measured initial real part ϵ' of the dielectric constant of the radome is around 2.5~2.6 (Fig.A.3). Considering the fact that the value of ϵ calculated by equation (A.3) is an approximation for the low-loss medium and the setting-up of the instrument as well as the orientation alignment of the sample is imperfect, the value of ϵ' is determined within 5% variation of the initial estimation, namely 2.375~2.73.

Substituting the whole tuned range of ϵ' into equation (2.22), comparing the theoretical reflectance to the measured mean reflectance of the radome and then the optimal estimation of ϵ' can be determined when the sum of squared residuals given by $L = \sum_{i=1}^n (y_i - x_i)^2$ is minimal, where x_i is the theoretical reflectance at each frequency element, y_i is the measured mean reflectance at each frequency element, n is the total number of frequency elements over the whole bandwidth. As to the dielectric loss factor, in the same way, the value of ϵ'' is tuned between 0~0.1 for the theoretical calculation of the transmittance of the single radome in equation (2.23) and the optimal estimation of ϵ'' can be obtained when the sum of squared residuals between theoretical and measured transmittance over the whole bandwidth is minimal.

For normal incidence, the resultant summation of the squared residuals for the reflectance and transmittance of the radome at each estimator of the real part of the dielectric constant (ϵ') and the loss factor (ϵ'') over the whole bandwidth is shown in Fig.A.5.

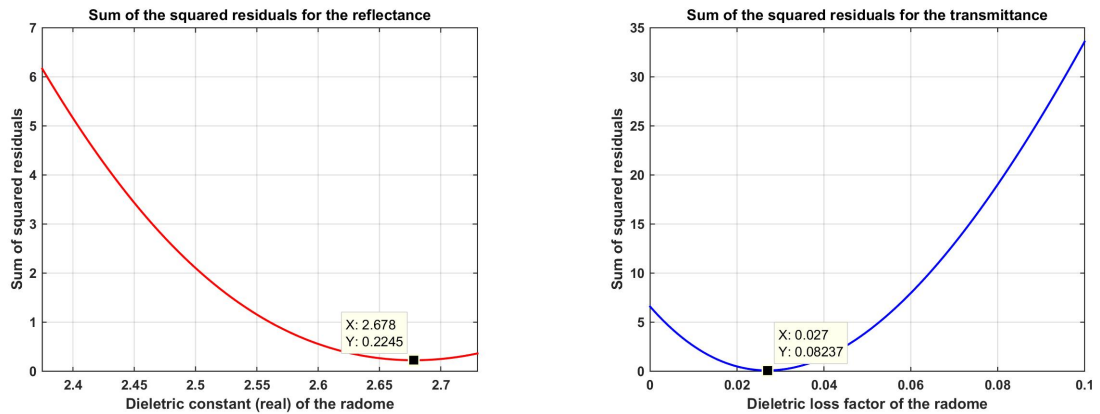


Figure A.5: Summations of the squared residuals for the reflectance and transmittance over the whole bandwidth

From Fig.A.5, it is observed that when the real part of the dielectric constant of the radome equals to 2.678 (left graph), the sum of the squared residuals for the reflectance between theoretical calculations and measurement results is minimal. In the same way, when the dielectric loss factor equals to 0.027, the sum of the squared residuals for the transmittance between theoretical calculations and measurement results is minimal. If we take $\epsilon = 2.678 - 0.027j$ as the radome dielectric constant, the comparisons between theoretical and measured reflectance and transmittance of the radome are shown in Fig.A.6.

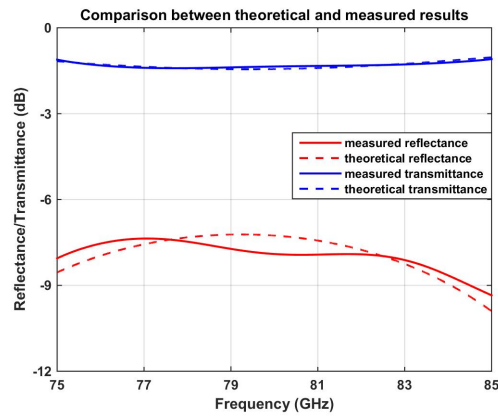


Figure A.6: Comparison between the theoretical and measured reflectance and transmittance of the radome

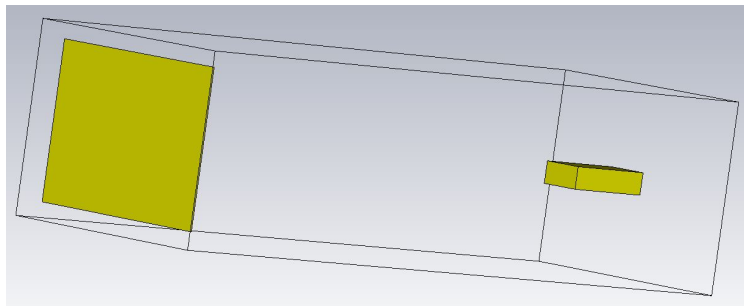
From Fig.A.6, we can see the bias between theoretical reflectance and measured reflectance of the radome is less than 1dB over the whole frequency band. As to the transmittance of the radome, the theoretical curve (blue, dotted line) is almost overlapped with the measured curve (blue, solid line). Thus there is roughly no bias between the theoretical and measured transmittance of the radome. Based on these results, the estimated dielectric permittivity of the radome $\epsilon = 2.678 - 0.027j$ is reasonable and this value is critical for the derivation of theoretical and numerical (CST) models for the wave propagation on the wet radome .

B

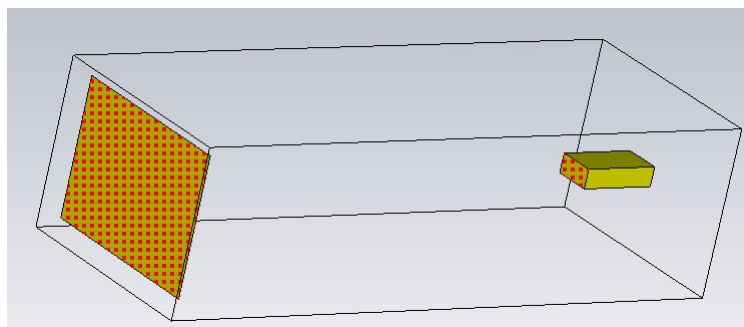
NUMERICAL MODEL IN CST

In this section, the specific steps for the modeling of wave propagation on the wet radome in CST are provided.

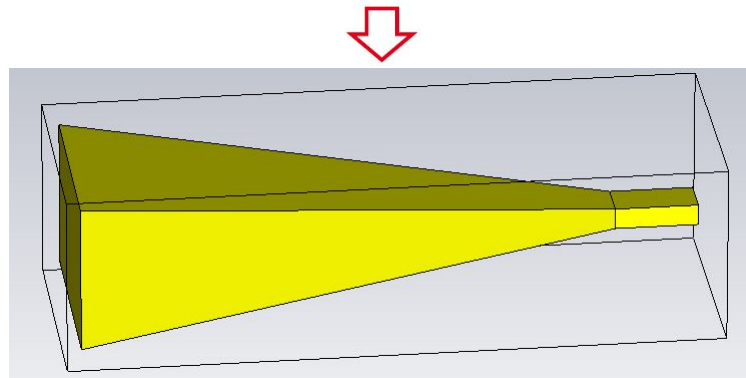
B.1. MODELING OF THE HORN ANTENNA



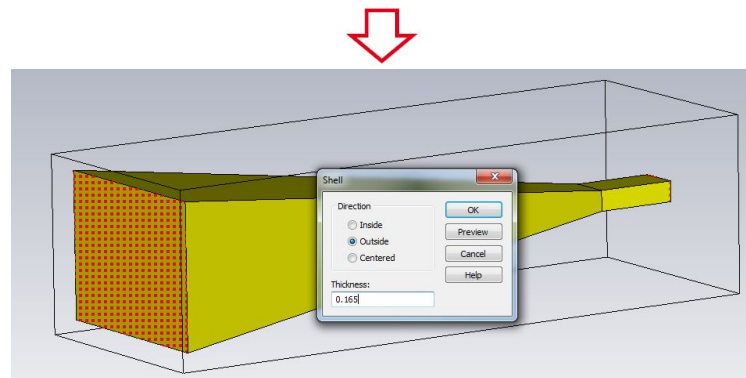
(a) Define the brick ($0.254\text{cm} \times 0.127\text{cm} \times 0.5\text{cm}$) and an analytical surface($1.24\text{cm} \times 0.9\text{cm}$)



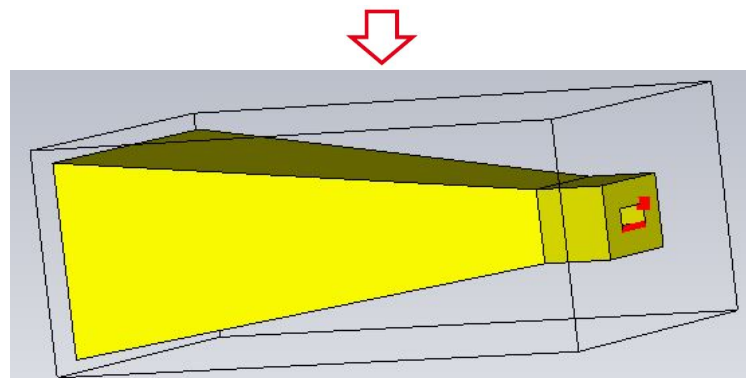
(b) Pick two opposite faces



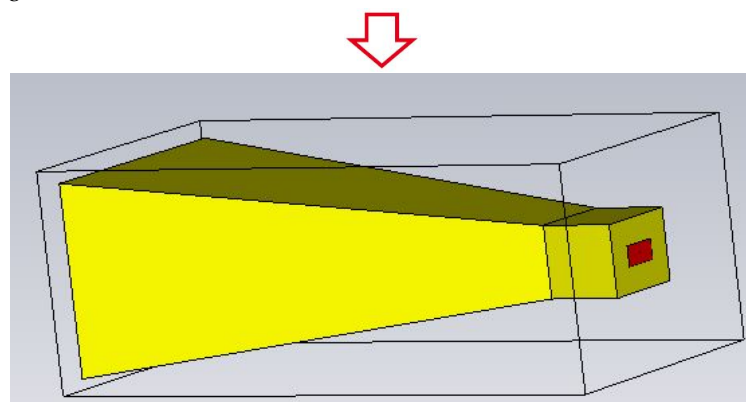
(c) Perform the loft



(d) Perform the Boolean add and then pick two faces, setting the thickness of shell solid



(e) Pick a point and edge inside the corner



(f) Define the waveguide port

Figure B.1: Modeling of the single horn antenna in CST

B.2. MODELING OF THE WET RADOME

After completing the modeling of the single horn antenna in section B.1, two horn antennas can be obtained by performing the mirror function. As to the modelings of the radome and the constant water film on the surface of the radome, the steps are shown in Fig.B.2 and Fig.B.3 respectively.

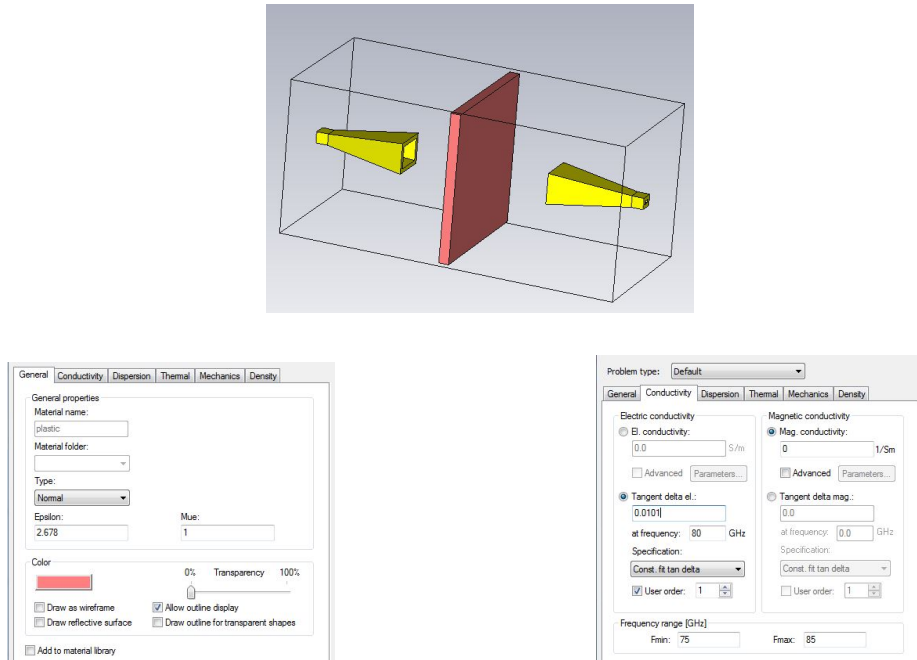


Figure B.2: Modeling of the radome (2.678-0.027) in CST

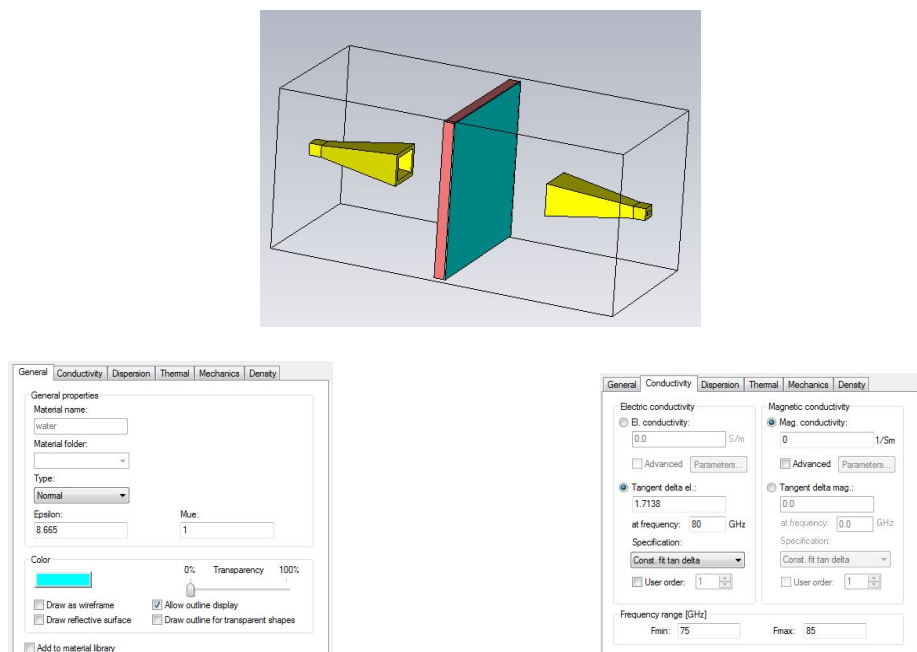


Figure B.3: Modeling of the water film in CST

C

SCRIPT FOR THE THEORETICAL MODEL

Listing C.1: MATLAB code for the theoretical model

```
clear all;
%% model: air-plastic-water-air
%% model: layer 1: plastic ,d1,eps1;    layer 2: water ,d2,eps;
d1=4.01e-3;
eps1=2.678-0.027j;
d2=0.51e-3;
theta0=0;
f=75:0.001:85;
theta0 = degtorad(theta0);
c0=3e8;
load ('eps.mat');
%% refractive index at each region
eps=conj(eps);
n0=1;
n1=sqrt(eps1);
n2=sqrt(eps);
n3=1;
%% incident angle at each region
theta1=asin(n0*sin(theta0)/n1);
theta2=asin(n0*sin(theta0)/n2);
theta3=asin(n0*sin(theta0)/n3);
%% wave number along z direction within layer 1-3
k1z=2*pi*f*n1/c0*cos(theta1)*1e9;
k2z=2*pi*f.*n2/c0.*cos(theta2)*1e9;
k3z=2*pi*f*n3/c0*cos(theta3)*1e9;
%% for TE wave, the reflection/transmission coefficient at each interface
r1_te=(n0*cos(theta0)-n1*cos(theta1))/(n0*cos(theta0)+n1*cos(theta1));
r2_te=(n1*cos(theta1)-n2.*cos(theta2))./(n1*cos(theta1)+n2.*cos(theta2));
r3_te=(n2.*cos(theta2)-n3*cos(theta3))./(n2.*cos(theta2)+n3*cos(theta3));
t1_te=1+r1_te;
t2_te=1+r2_te;
t3_te=1+r3_te;
```

```

%% for TM wave, the refecton coefficient
r1_tm=(n0*cos(theta1)-n1*cos(theta0))/(n0*cos(theta1)+n1*cos(theta0));
r2_tm=(n1*cos(theta2)-n2*cos(theta1))/(n1*cos(theta2)+n2*cos(theta1));
r3_tm=(n2*cos(theta3)-n3*cos(theta2))/(n2*cos(theta3)+n3*cos(theta2));
t1_tm=2*n0*cos(theta0)/(n0*cos(theta1)+n1*cos(theta0));
t2_tm=2*n1*cos(theta1)/(n1*cos(theta2)+n2*cos(theta1));
t3_tm=2*n2*cos(theta2)/(n2*cos(theta3)+n3*cos(theta2));
%% propagation matrix
C_te=zeros(2,2,length(eps));
C_tm=zeros(2,2,length(eps));
R_te=zeros(1,length(eps));
T_te=zeros(1,length(eps));
R_tm=zeros(1,length(eps));
T_tm=zeros(1,length(eps));
for m=1:length(eps)
    C_te(:, :, m)=[1 r1_te; r1_te 1]*[exp(-1i*(k2z(1,m)-k1z(1,m))*d1) r2_te(1,m)*...
        exp(1i*(k2z(1,m)+k1z(1,m))*d1); r2_te(1,m)*exp(-1i*(k2z(1,m)+k1z(1,m))*...
        d1) exp(1i*(k2z(1,m)-k1z(1,m))*d1)];* [exp(-1i*(k3z(1,m)-k2z(1,m))*...
        (d1+d2)) r3_te(1,m)*exp(1i*(k3z(1,m)+k2z(1,m))*(d1+d2)); r3_te(1,m)*...
        exp(-1i*(k3z(1,m)+k2z(1,m))*(d1+d2)) exp(1i*(k3z(1,m)-k2z(1,m))*(d1+d2))];];

    C_tm(:, :, m)=[1 r1_tm; r1_tm 1]*[exp(-1i*(k2z(1,m)-k1z(1,m))*d1) r2_tm(1,m)*...
        exp(1i*(k2z(1,m)+k1z(1,m))*d1); r2_tm(1,m)*exp(-1i*(k2z(1,m)+k1z(1,m))*...
        d1) exp(1i*(k2z(1,m)-k1z(1,m))*d1)];* [exp(-1i*(k3z(1,m)-k2z(1,m))*...
        (d1+d2)) r3_tm(1,m)*exp(1i*(k3z(1,m)+k2z(1,m))*(d1+d2)); r3_tm(1,m)*...
        exp(-1i*(k3z(1,m)+k2z(1,m))*(d1+d2)) exp(1i*(k3z(1,m)-k2z(1,m))*(d1+d2))];];

%% reflection/transmission coefficient calculation
R_te(1,m)=C_te(2,1,m)/C_te(1,1,m);
T_te(1,m)=t1_te*t2_te(1,m)*t3_te(1,m)/C_te(1,1,m);
R_tm(1,m)=C_tm(2,1,m)/C_tm(1,1,m);
T_tm(1,m)=t1_tm*t2_tm(1,m)*t3_tm(1,m)/C_tm(1,1,m);
end
%% reflectivity/transmissivity calculation
Ref_te=abs(R_te).^2;
Tra_te=abs(T_te).^2*n3*cos(theta3)/n0./cos(theta0);
Ref_tm=abs(R_tm).^2;
Tra_tm=abs(T_tm).^2*n3*cos(theta3)/n0./cos(theta0);
%% plots on reflectivity/transmissivity
Ref_te=10*log10(Ref_te);
Ref_tm=10*log10(Ref_tm);
Tra_te=10*log10(Tra_te);
Tra_tm=10*log10(Tra_tm);
figure (1)
plot(f,(Ref_te), 'r', f,(Tra_te), 'b', 'LineWidth', 1.5);
legend('Reflectivity', 'Transmissivity')
title('H-Polarization')
xlabel('Frequency_(GHz)')
ylabel('Reflectivity/Transmissivity')
grid on;

```

```
axis([75 85 -30 0])  
figure (2)  
plot(f,(Ref_tm), 'r',f,(Tra_tm), 'b', 'LineWidth',1.5);  
legend(' Reflectivity', 'Transmissivity')  
title(' relative_permitivity_(2.6-0.022j)')  
xlabel('Frequency_(GHz)')  
ylabel(' Reflectivity/Transmissivity')  
grid on;  
axis([75 85 -30 0])
```


D

SCRIPT FOR THE NUMERICAL MODEL

Listing D.1: MATLAB code to process the data from CST simulation

```
clear all;  
%%load the data from CST.  
[f,s22_r]=textread('s22_6.5_1layer_r.txt','%f%f','headerlines',2);  
[f,s22_i]=textread('s22_6.5_1layer_i.txt','%f%f','headerlines',2);  
s22_new=s22_r+1i*s22_i;  
  
%% transfer the data from frequency domain to the time domain  
f=f*1e9;  
df=f(2)-f(1);  
f2=[df:df:f(1)-df];  
f1=[f2 f.'];  
nf=f(1)/df;  
s22_zeros=zeros(floor(nf)-1,1);  
s22=[s22_zeros;s22_new];  
s22_t=(length(s22)/length(f)).*ifft(s22);  
tt=[0:length(s22)-1].*(1/(f(end)));  
dd=3e8*tt/2;  
figure (11)  
plot(tt*1e9,20*log10(abs(s22_t(:,1))), 'r')  
axis([0 10 -60 0])  
  
%% Gating the other interfering signals  
%% and then transfer it back to the frequency domain  
[r,c]=size(s22_t);  
s22_t_new=zeros(r,c);  
s22_t_new(30:54,:)=s22_t(30:54,:);  
s22_f=fft(s22_t_new)./(length(s22)/length(f));  
figure (22)  
plot(f1*1e-9,20*log10(abs(s22_f)), 'g')  
axis([75 85 -30 0])  
grid on;
```


BIBLIOGRAPHY

- [1] L. Hasch and C. Waldschmidt, *In safety for all*, Europe Radar Conf. Workshop WFF01 (2010).
- [2] A. Alebel, *Indicators for the signal degradation and optimization of automotive radar sensors under adverse weather conditions*, Ph.D dissertation, TU Darmstadt (2006).
- [3] R. Schnabel, D. Mittelstra, T. Binzer, C. Waldschmidt, and R. Weigel, *Reflection, refraction and self-jamming*, [IEEE microwave magazine](#) , 107 (2012).
- [4] O. Heavens, *Optical properties of thin solid films*, Courier Corporation (1991).
- [5] C. Bishop, *The relationship between loss, conductivity and dielectric constant*, (2001).
- [6] C. Balanis, *Advanced engineering electromagnetics*, 2nd Edition, Wiley (2012).
- [7] F. Ulaby and D. Long, *Microwave radar and radiometric remote sensing*, University of Michigan Press (2013).
- [8] M. Kurri and A. Huuskonen, *Measurements of the transmission loss of a radome at different rain intensities*, [Atmospheric and Ocean Technology](#) , 1590 (2012).
- [9] R. Olmi, M. Tedesco, C. Riminesi, and A. Ignest, *Thickness-independent measurement of the permittivity of thin samples in the x band*, [Measurement Science and Technology](#) , 503 (2002).
- [10] C. Balanis, *Antenna theory*, 2nd ed. New York: Wiley (1997).
- [11] *Standard gain horns series 240*, [Online]. Available: www.flann.com .
- [12] B. Burmann, *Specifications for the secondary surface for the 77ghz automotive radar*, Profit Center Driver Assistance Systems (2006).
- [13] R. Liebske, *Short range radar sensor*, Continental (2013).
- [14] I. Hajnsek and K. Papathanassiou, *Rough surface scattering models*, [Online]. Available: <https://earth.esa.int/documents/653194/656796> .
- [15] F. Bass and I. Fuks, *Wave scattering from statistically rough surfaces*, Institute of Radiophysics and Electronics, Kharkov, USSR .
- [16] N. Zhuk, O. Tretyakov, I. Fuks, and A. Yarovoi, *Thermal radio emission of a homogeneous half-space with a rough boundary*, Plenum Publishing Corporation (1990).
- [17] A. Fung, *Microwave scattering and emission models and their applications*, Boston: Artech House (1994).
- [18] M. Richards, J. Scheer, and W. Holm, *Principles of modern radar*, The Institution of Engineering and Technology (2010).
- [19] S. Orfanidis, *Electromagnetic waves and antennas*, ECE Department, Rutgers University (2002).
- [20] S. Trabelsi, A. Kraszewski, and O. Nelson, *Phase-shift ambiguity in microwave dielectric properties measurements*, [IEEE Transactions on Instrumentation and Measurement](#) , 56 (2000).